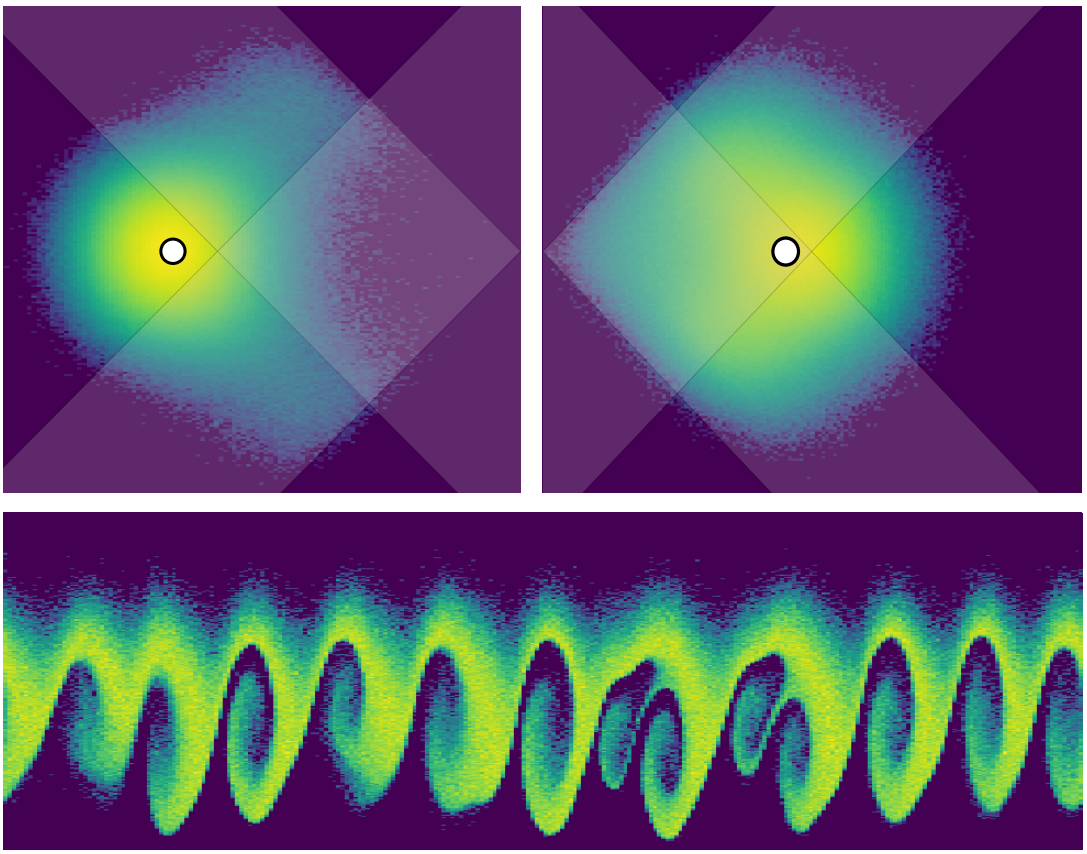

Kinetic Simulations of the Proton-Alpha Instability in Collisionless Shocks

Master's thesis in Complex Adaptive Systems

NILS MÜLLER

DEPARTMENT OF PHYSICS
CHALMERS UNIVERSITY OF TECHNOLOGY
Gothenburg, Sweden 2025
www.chalmers.se

Master's thesis 2025

Kinetic Simulations of the Proton-Alpha Instability in Collisionless Shocks

NILS MÜLLER

CHALMERS
UNIVERSITY OF TECHNOLOGY

Department of Physics
Division of Subatomic, High Energy and Plasma Physics
Chalmers University of Technology
Gothenburg, Sweden 2025

Kinetic Simulations of the Proton-Alpha Instability in Collisionless Shocks
NILS MÜLLER

© NILS MÜLLER, 2025.

Supervisor: Konrad Steinvall, Department of Physics
Examiner: István Pusztai, Department of Physics

Master's Thesis 2025
Department of Physics
Division of Subatomic, High Energy and Plasma Physics
Chalmers University of Technology
SE-412 96 Gothenburg
Telephone +46 31 772 1000

Cover: Visualization of the proton (left) and alpha (right) distribution functions in velocity space, with trapping regions from theory (transparent bands) at the end of the linear growth phase. The lower subplot shows the distribution function of the protons in a one-dimensional simulation at the same time.

Acknowledgements, dedications, and similar personal statements in this thesis, reflect the author's own views.

Printed by Chalmers Reproservice
Gothenburg, Sweden 2025

Kinetic Simulations of the Proton-Alpha Instability in Collisionless Shocks

NILS MÜLLER
Department of Physics
Chalmers University of Technology

Abstract

The solar wind is a dynamic stream of collisionless plasma originating from the Sun. When it reaches the Earth's magnetosphere, it abruptly slows down from super-Alfvénic to sub-Alfvénic speeds, creating a bow shock. This compresses and heats the inflowing plasma. The solar wind consists primarily of electrons, protons and alpha-particles, which interact differently with the shock. A relative drift between protons and alpha particles develops, which can trigger a streaming instability, driving waves. Such waves have previously been identified in spacecraft observations. The dependence of the instability on the particle species temperature, density, and flow velocity has previously been investigated using the dispersion relation for an unmagnetized plasma.

In this work, we investigate this proton-alpha streaming instability using two-dimensional fully kinetic Particle-In-Cell simulations. This approach offers the flexibility to freely choose the initial conditions while simulating the full non-linear dynamics. We study the parametric dependence of the instability on the flow velocity of the alpha particles, the density ratio of the ions as well as the influence of a background magnetic field. In particular, we want to quantify the heating of different particle species due to the instability. Additionally, we aim to test the applicability of the simplified linear theory.

Our simulations show that the instability mediates a strong energy exchange from the flow speed of the alphas into plasma heating of the ions. We attribute this to a Landau resonance between the proton and the alpha distribution, which produces large plateaus in velocity space. The electron dynamics do not change significantly. The wave properties are consistent with the linear theory when the external magnetic field is small. Generally, the angle between the wave and the drift direction increases with the flow speed. The fraction of energy converted to plasma heating reaches a maximum at a wave angle of 45 deg to the drift direction. Overall, the existence of a background magnetic field slightly suppresses the instability, due to the magnetization of electrons. We conclude that the proton-alpha streaming instability can play an important role in heating protons and alpha particles across collisionless shocks.

Keywords: Kinetic simulation, Ion-ion instability, Bow shock, Solar wind, Plasma waves

Acknowledgements

First and foremost, a big thank you to my supervisor, Konrad Steinvall, for all the help, guidance, and support throughout the project. I really enjoyed working with you and learned a lot along the way. I'm also grateful to my examiner, István Pusztai, for his valuable feedback and thoughtful input, which really helped improve the thesis. I would also like to thank Tünde Fülöp for making this project possible in the first place—your support and initiative are very much appreciated. A big thank you to the whole research group for welcoming me so warmly and making my time here so enjoyable and memorable. Our regular fika breaks were a highlight of my days and a great way to take a pause and connect.

Lastly, I want to thank my girlfriend and my family for the constant encouragement, the support, and for all the wonderful time I get to spend with you.

The computations were enabled by resources provided by the National Academic Infrastructure for Supercomputing in Sweden (NAISS), partially funded by the Swedish Research Council through grant agreement no. 2022-06725. The EPOCH code used in this work was in part funded by the UK EPSRC grants EP/G054950/1, EP/G056803/1, EP/G055165/1, EP/ M022463/1 and EP/P02212X/1.

Nils Müller, Gothenburg, 2025-6

Nomenclature

Below is the nomenclature of indices, parameters, and variables that have been used throughout this thesis.

Indices

e	Electron particle species
p	Proton particle species
α	Alpha particle species
s	Particle species index
x, y, z	Cartesian spatial coordinates

Constants

i	Imaginary unit
k_B	Boltzmann constant
ϵ_0	Vacuum permittivity
q	Charge
m	Mass
λ_D	Debye length
$\omega_{\mathrm{p}s}$	Species plasma frequency
$v_{\mathrm{t}s}$	Species thermal speed
ω_r	Landau resoance velocity
γ	Growth rate
v_ph	Wave phase velocity
N_sim	Number of pseudoparticles
N_cell	Number of simulation cells
Δx	Side length of cells (in x)
Δy	Side length of cells (in y)
Δt	Time between simulation captures
Δt_sim	Time between simulation steps

Variables

t	Time
$\boldsymbol{r}$	Position
$\boldsymbol{v}$	Velocity
$\boldsymbol{p}$	Momentum
$\boldsymbol{u}$	Flow velocity
$\boldsymbol{k}$	Wave vector
ω	Wave frequency
θ	Wave angle
f	Spcies distribution function
T	Temperature
K	Kinetic energy
ρ	Charge density
n	Number density
ϕ	Electric potential
$\boldsymbol{E}$	Electric field
$\boldsymbol{B}$	Magnetic field
W_E	Electric field energy
W_s	Species energy
K_s	Species kinetic energy
$\langle\cdot\rangle$	Average of $\cdot$
$\nabla_\cdot$	Gradient with respect to $\cdot$
$\nabla\cdot$	Divergence operator
$\mathcal{F}$	Fourier transform
$\mathcal{Z}$	Plasma dispersion function
δ	Dirac-Delta distribution

Contents

List of Figures

List of Tables

1

Introduction

All planets in the solar system, including the Earth, are embedded in a dynamic stream of plasma known as the solar wind (Owens, 2020). It flows away from the Sun and fills the entire heliosphere. Generally, this stream is super-Alfvénic (Lalti et al., 2022; Owens, 2020), which means that the bulk flow of the solar wind is faster than the propagation speed of large scale magnetic perturbations. However, at some distance from the Earth (usually around 12 Earth radii) (Merka et al., 2005), the Earth's magnetic field is strong enough to act as an obstacle and abruptly slow down the solar wind (Balogh et al., 2013). Here, the bulk velocity of the plasma stream decreases from super-Alfvénic to sub-Alfvénic speeds and a bow shock forms. The bow shock compresses the plasma, causing the temperature and density of the shocked plasma to increase (Balogh et al., 2013; Merka et al., 2005). This phenomenon is particularly interesting to study when a large quantity of high-velocity plasma is emitted from the Sun during a coronal mass ejection (CME) (Webb et al., 2012). During such events, we are able to explore the plasma dynamics in parameter regions which deviate from the usual conditions in the Earth's bow shock.

The solar wind consists primarily of electrons, protons, and alpha particles (Bame et al., 1968) and is classified as a collisionless plasma (Coburn et al., 2022; Kennel et al., 1985). This means that the mean free path is much larger than the spatial extent of the system. In such a plasma, particle dynamics are dominated by electromagnetic interactions via the Lorentz force. The governing equation of this system is given by

$$\boldsymbol{F}_{\text{lorentz}} = m_s \frac{d\boldsymbol{v}}{dt} = q_s(\boldsymbol{E} + \boldsymbol{v} \times \boldsymbol{B}), \tag{1.1}$$

where m_s and q_s are the mass and charge of the particle species. $\boldsymbol{E}$ and $\boldsymbol{B}$ are the electric and magnetic fields, respectively. Equation (1.1) shows that the dynamics depend on the charge-to-mass ratio q_s/m_s of the respective species. As a result, the heating process, length scale and interaction with the shock generally may also depend on the species (Fuselier et al., 1994).

The goal of this work is to investigate a part of the ion dynamics downstream of the Earth's bow shock. Previously, Graham et al., 2024 identified the formation of large-amplitude plasma waves in the observations from the Magnetospheric Multiscale (MMS) mission (Burch et al., 2015). These waves form through a strong interaction between protons and alpha particles due to their relative drift (Graham et al., 2025). Over time, the high bulk velocity of the alpha particles decreases, as the energy is converted to collisionless plasma heating. Generally, the discov-

ered phenomenon can be characterized as a streaming instability (Graham et al., 2025; Swanson, 2003). Graham et al., 2025 developed a theoretical model which can describe its initial, linear phase.

In this work, we aim to go beyond the linear phase and learn more about the entire spatial and temporal evolution. We aim to address the following questions: How much are the different particle species in the plasma heated? How do the dynamics depend on the strength and direction of the background magnetic field? How does this change for different bulk velocities of the alpha particles or when their number density changes? Are the dynamics of the electrons affected as well?

These questions cannot be answered through linear plasma theory. The resolution and quality of present observations are constrained by the spacecrafts' instruments (Burch et al., 2015; Pollock et al., 2016). Additionally, observations are intermittent and only available while the spacecrafts' trajectories intersect the bow shock region (Tooley et al., 2015). Finally, the rotational angular velocity and orientation of each spacecraft constrains the measurable solid angles (Tooley et al., 2015). To complement the available observations, we choose to simulate the plasma dynamics using EPOCH, a fully kinetic Particle-In-Cell (PIC) code (Arber et al., 2015). Here, plasma parameters like the temperatures and densities of individual species or the background magnetic field can be freely varied (Arber et al., 2015; Birdsall et al., 2018; Dijk et al., 2009). We can measure the full, time-resolved distribution functions, as well as electric and magnetic fields at high resolution. This enormous flexibility entails a considerable computational cost required to reduce the simulation noise and avoid numerical instabilities (Arber et al., 2015; Courant et al., 1928; Engquist et al., 2012; Yee, 1966).

The structure of this work is as follows: Chapter 2 provides a fundamental understanding of plasma waves, their properties, and behaviour. This is required to explain the origin and theory behind the proton-alpha instability which is introduced thereafter. Next, chapter 3 gives an overview of the PIC simulation method. The gained insight into the PIC method also aims to emphasize the dependence of its capabilities on the available computational resources. We will present and discuss the captured simulation data in chapter 4 with the aim to answer the previously posed questions. Finally, chapter 5 summarizes our conclusions based on the findings in chapter 4 and poses new questions for future research.

2

Theoretical background

This chapter provides the theoretical background necessary to understand the physics behind the proton-alpha instability. We start with a brief introduction to plasma waves by examining the dispersion relation of the Langmuir plasma oscillation. Subsequently, an explanation of Landau resonance and its associated theoretical predictions provides insight into the emergence of plasma instabilities. Finally, we go into more detail about the proton-alpha instability, with a focus on its origin and the linear theory. Numerical solutions of the dispersion relation show how the wave properties change under different plasma parameters.

2.1 Plasma waves

Plasma waves arise as collective oscillations of charged particles interacting via electromagnetic fields. In this section, we introduce the most important concepts in the kinetic theory of plasma waves. A more extensive study of the field of plasma waves can, among other textbooks, be found in Swanson, 2003. In addition to the Maxwell equations, we will use the Vlasov equation

$$\frac{\partial f_s}{\partial t} + \boldsymbol{v} \cdot \nabla f_s + \frac{q_s}{m_s} (\boldsymbol{E} + \boldsymbol{v} \times \boldsymbol{B}) \cdot \nabla_{\boldsymbol{v}} f_s = 0. \tag{2.1}$$

Together, these equations provide a statistical description of the evolution of a collisionless plasma under some assumptions (Swanson, 2003). Firstly, interactions between individual particles are neglected. Instead, the motion of each particle is independently described by long-range interactions via the Lorentz force (cf. eq. (1.1)). Secondly, all particles of a species s are modelled via their distribution function $f_s(\boldsymbol{x}, \boldsymbol{v}, t)$. It determines the particle density in phase space $(x\, y\, z\, v_x\, v_y\, v_z)$ over time t.

2.1.1 Dispersion relation

Plasmas with different temperatures, particle species, magnetization, etc. contain a variety of plasma waves. In order to derive properties of these waves theoretically, we make a plane wave ansatz. The fundamental assumption is that the total wave is a sum of sinusoidal waves, which works well in a spatially homogeneous background[1].

[1] Due to high discretization noise, this assumption is not always satisfied in our simulations.

Sine waves are fully determined by their amplitude, angular wave vector $\boldsymbol{k}$ and angular frequency ω. The goal then becomes to find the dispersion relation, a function that constrains the possible ω for a given $\boldsymbol{k}$.

Perhaps the most universal type of plasma wave is called the plasma oscillation or Langmuir wave. It was discovered by Tonks et al., 1929. Here, we will use the plasma oscillation in an unmagnetized plasma ($\boldsymbol{B} = 0$) as an example to show the ansatz used to obtain a linear dispersion relation from the Vlasov equation.

The plasma oscillation (or Langmuir wave) is an electrostatic wave. This means that charge imbalances are the only source of electric fields. We can thus limit our system of equations to Gauss's law (the first Maxwell equation) and the Vlasov equation to obtain the following system of equations:

$$\frac{\partial f_s}{\partial t} + \boldsymbol{v} \cdot \nabla f_s + \frac{q_s}{m_s} \boldsymbol{E} \cdot \nabla_{\boldsymbol{v}} f_s = 0 \tag{2.2}$$

$$\nabla \cdot \boldsymbol{E} = -\nabla^2 \phi = \rho / \epsilon_0. \tag{2.3}$$

Here, ϕ is the electrostatic potential and ρ the charge density of the plasma. Now, we analyse what happens when the distribution function f_s is slightly perturbed from a spatially homogeneous equilibrium $f_{s0}(\boldsymbol{v})$. In first order perturbation theory (linear theory), the expansions $f_s(\boldsymbol{x}, \boldsymbol{v}, t) \to f_{s0}(\boldsymbol{v}) + f_{s1}(\boldsymbol{x}, \boldsymbol{v}, t)$ and $\phi \to \phi_0 + \phi_1(\boldsymbol{x}, t)$ yield a simplified Vlasov equation (using Gauss's law) for each species:

$$\frac{\partial f_{s1}}{\partial t} + \boldsymbol{v} \cdot \nabla f_{s1} - \frac{q_s}{m_s} \nabla \phi_1 \cdot \nabla_{\boldsymbol{v}} f_{s0} = 0. \tag{2.4}$$

At this point, we utilize the plane wave approximation by applying the Fourier transformation $\mathcal{F}$ to f_{s1} and ϕ_1:

$$\mathcal{F}(f_{s1}(\boldsymbol{x}, \boldsymbol{v}, t)) = \tilde{f}_{s1}(\boldsymbol{k}, \boldsymbol{v}, \omega)$$
$$\mathcal{F}(\phi_1(\boldsymbol{x}, t)) = \tilde{\phi}_{s1}(\boldsymbol{k}, \omega).$$

Equation (2.4) in terms of $\tilde{f}_{s1}$ and $\tilde{\phi}_1$ is rearranged for $\tilde{f}_{s1}$:

$$(-i\omega + i\boldsymbol{k} \cdot \boldsymbol{v}) \tilde{f}_{s1} = \frac{q_s}{m_s} i \tilde{\phi}_1 \boldsymbol{k} \cdot \nabla_{\boldsymbol{v}} f_{s0}$$
$$\iff \tilde{f}_{s1} = \frac{q_s \boldsymbol{k} \cdot \nabla_{\boldsymbol{v}} f_{s0}}{m_s (\boldsymbol{k} \cdot \boldsymbol{v} - \omega)} \tilde{\phi}_1$$

Equation (2.3), the Poisson equation, relates the electric potential ϕ_1 to the charge density $\rho = \sum_s q_s (n_{s0} + n_{s1})$ which is a linear superposition of the charge density of every species. Here, n_{s0} and n_{s1} are the background and perturbed number density, respectively. For simplicity, we consider a plasma where $\rho = q_\mathrm{e} n_{\mathrm{e}1}$, i.e. all species except the electrons are stationary[2] with $n_{s1} = 0$ and the background is neutral with $\sum_s q_s n_{s0} = 0$[3]. This finally leads us to the unmagnetized plasma dispersion relation

[2]This assumption is also physically motivated: Due to their low mass, the electron mobility is much higher than that of the ions.

[3]If one drops the assumption that the other species are stationary, this leads to a sum over all species s in eq. (2.5).

(for the electrons):

$$\begin{aligned}
\nabla^2\phi_1 &= -\rho/\epsilon_0 \\
\Rightarrow (i\boldsymbol{k})^2\tilde{\phi}_1 &= -\frac{q_\mathrm{e}}{\epsilon_0}n_{\mathrm{e}1} \\
\Rightarrow k^2\tilde{\phi}_1 &= \frac{q_\mathrm{e}}{\epsilon_0}\int d^3v\,\tilde{f}_{\mathrm{e}1} \\
\Rightarrow k^2\tilde{\phi}_1 &= \frac{q_\mathrm{e}}{\epsilon_0}\int d^3v\,\frac{q_\mathrm{e}\boldsymbol{k}\cdot\nabla_{\boldsymbol{v}}f_{\mathrm{e}0}}{m_\mathrm{e}(\boldsymbol{k}\cdot\boldsymbol{v}-\omega)}\tilde{\phi}_1 \\
\iff 1 &= \frac{q_\mathrm{e}^2}{k^2 m_\mathrm{e}\epsilon_0}\int d^3v\,\frac{\boldsymbol{k}\cdot\nabla_{\boldsymbol{v}}f_{\mathrm{e}0}}{\boldsymbol{k}\cdot\boldsymbol{v}-\omega}.
\end{aligned} \tag{2.5}$$

In the cold plasma limit, we assume that the electron temperature T_e goes to zero $T_\mathrm{e}\to 0$ which yields the equilibrium $f_{\mathrm{e}0}(\boldsymbol{v}) = n_\mathrm{e}\delta(\boldsymbol{v})$ in terms of the electron number density n_e[4]. This allows us to solve the integral in eq. (2.5) to obtain the specific dispersion relation of the electron plasma oscillation:

$$\begin{aligned}
1 &= \frac{q_\mathrm{e}^2}{k^2 m_\mathrm{e}\epsilon_0}\int d^3v\,\frac{\boldsymbol{k}\cdot\nabla_{\boldsymbol{v}}f_{\mathrm{e}0}}{\boldsymbol{k}\cdot\boldsymbol{v}-\omega} \\
&= \frac{q_\mathrm{e}^2 n_\mathrm{e}}{k^2 m_\mathrm{e}\epsilon_0}\int d^3v\,\frac{\boldsymbol{k}\cdot\nabla_{\boldsymbol{v}}\delta(\boldsymbol{v})}{\boldsymbol{k}\cdot\boldsymbol{v}-\omega} \\
&= \frac{q_\mathrm{e}^2 n_\mathrm{e}}{k^2 m_\mathrm{e}\epsilon_0}\frac{k^2}{(\omega-\boldsymbol{k}\cdot\boldsymbol{v})^2}\bigg|_{\boldsymbol{v}=0} \\
1 &= \frac{q_\mathrm{e}^2 n_\mathrm{e}}{m_\mathrm{e}\epsilon_0}\frac{1}{\omega^2} \\
\Rightarrow \omega^2 &= \omega_\mathrm{pe}^2 = \frac{q_\mathrm{e}^2 n_\mathrm{e}}{m_\mathrm{e}\epsilon_0}.
\end{aligned} \tag{2.6}$$

Here, we used the identity $\int dx\, g(x)\delta'(x) = -g'(0)$ to solve the integral. We call ω_pe the electron plasma frequency. Notice that for the plasma oscillation, the dispersion relation does not depend on $\boldsymbol{k}$. All wave modes oscillate at the same frequency, independent of the wavelength. In conclusion, plasma oscillations do not propagate. Instead, the particles oscillate around their equilibrium position. Finally, as the plasma oscillation also occurs for other species, the electron plasma frequency is generalized to the plasma frequency $\omega_{\mathrm{p}s}$ of a given species s. In fact, the plasma oscillation is so ubiquitous that the plasma frequency $\omega_{\mathrm{p}s}$ provides a fundamental characteristic timescale of the plasma. It is complemented by the Debye length λ_D, a length scale for the shielding of individual electrostatic charges in the plasma. In this thesis, we will use the Debye length of an isothermal plasma

$$\lambda_\mathrm{D} = \left(\frac{\epsilon_0 k_\mathrm{B} T}{\sum_s n_s q_s^2}\right)^{1/2}. \tag{2.7}$$

For other velocity distribution functions (VDFs), the evaluation of eq. (2.5) is more complicated. Let us consider $f_{\mathrm{e}0}$ to be the Maxwell-Boltzmann distribution

[4]The Dirac delta distribution $\delta(x)$ is defined as $\delta(0) = \infty$ and zero elsewhere such that $\int \delta(x)\,dx = 1$.

with a flow speed u_e. Now, the dispersion relation takes the form (Gary, 1979; Swanson, 2003)

$$1 = \frac{\omega_\mathrm{pe}^2}{\boldsymbol{k}^2 v_\mathrm{te}^2} \mathcal{Z}' \left(\frac{\omega - k_\parallel \cdot u_\mathrm{e}}{k v_\mathrm{te}} \right) \tag{2.8}$$

$$\text{with} \quad \mathcal{Z}'(\zeta) = \frac{d\mathcal{Z}}{d\zeta}(\zeta) = \frac{1}{\sqrt{\pi}} \int_{-\infty}^{\infty} dt \frac{\exp(-t^2)}{(t-\zeta)^2}. \tag{2.9}$$

$\mathcal{Z}$ is called the plasma dispersion function (Fried et al., 2015). The thermal speed $v_\mathrm{te} = \sqrt{2 k_\mathrm{B} T_e / m_e}$ is defined as the most probable speed. Equation (2.9) is a complex-valued non-linear equation that depends on four real scalar variables: Firstly, $\boldsymbol{k} = (k_\parallel, k_\perp, 0)$ determines the wave's direction[5]. Secondly, $\omega = \omega_\mathrm{r} + \gamma i$ consists of the wave's frequency ω_r and growth rate $\gamma > 0$. Note that for $\gamma < 0$, the Vlasov-Maxwell equation has a stable steady state in which there is no oscillatory solution, and any perturbations will exponentially decay. Periodic oscillations like the electron plasma oscillation with marginal stability (neither growth nor decay) form at $\gamma = 0$. For the case $\gamma > 0$, the amplitude of the waves grows exponentially from the initially small perturbation until it enters a non-linear regime where the first order perturbation theory no longer holds.

2.1.2 Landau resonance

Landau resonance is a resonance that appears because individual particles exchange energy with a plasma wave, which can make it grow or decay (Landau, 1946). Therefore, Landau resonance relies on a kinetic description of the plasma-like the system of Vlasov-Maxwell equations. This is opposed to fluid descriptions: These do not model individual particles and, thereby, cannot explain the Landau resonance phenomenon.

We want to consider a one-dimensional model to obtain an intuition for the phenomenon: Particles with velocity v that are slightly slower than the phase velocity v_ph of the wave ($v < v_\mathrm{ph}$) will on average be accelerated by the wave electric field. As a result, the wave loses energy while the particle gains energy (wave damping). The situation is inverted for slightly faster particles ($v > v_\mathrm{ph}$) which are on average decelerated and transfer energy to the wave (wave growth). The particles that have velocities $v \approx v_\mathrm{ph}$ are effectively trapped and oscillate between two adjacent wavefronts. Thus, this range of velocities is called the trapping range. Finally, the interaction between the wave and particles with $v \ll v_\mathrm{ph}$ or $v \gg v_\mathrm{ph}$ is negligible. Figure 2.1 uses the results from a simulation of the particle dynamics in an electrostatic wave to illustrate the phenomenon. The electric potential ϕ (upper subplot) acts as a potential well which divides the phase space near v_ph. In the centre subplot we can clearly distinguish trapped, elliptical, particle trajectories from those which only experience minor perturbations due to the plasma wave.

Now, let us zoom out to the overall change in the VDF f_s: We find that perturbations in f_s will grow where the velocity gradient is positive (Landau growth

[5] In our case, the drift in the x-direction, so the standard Cartesian coordinate system is sufficient to represent $\boldsymbol{k}$ via $k_\parallel$ and $k_\perp$.

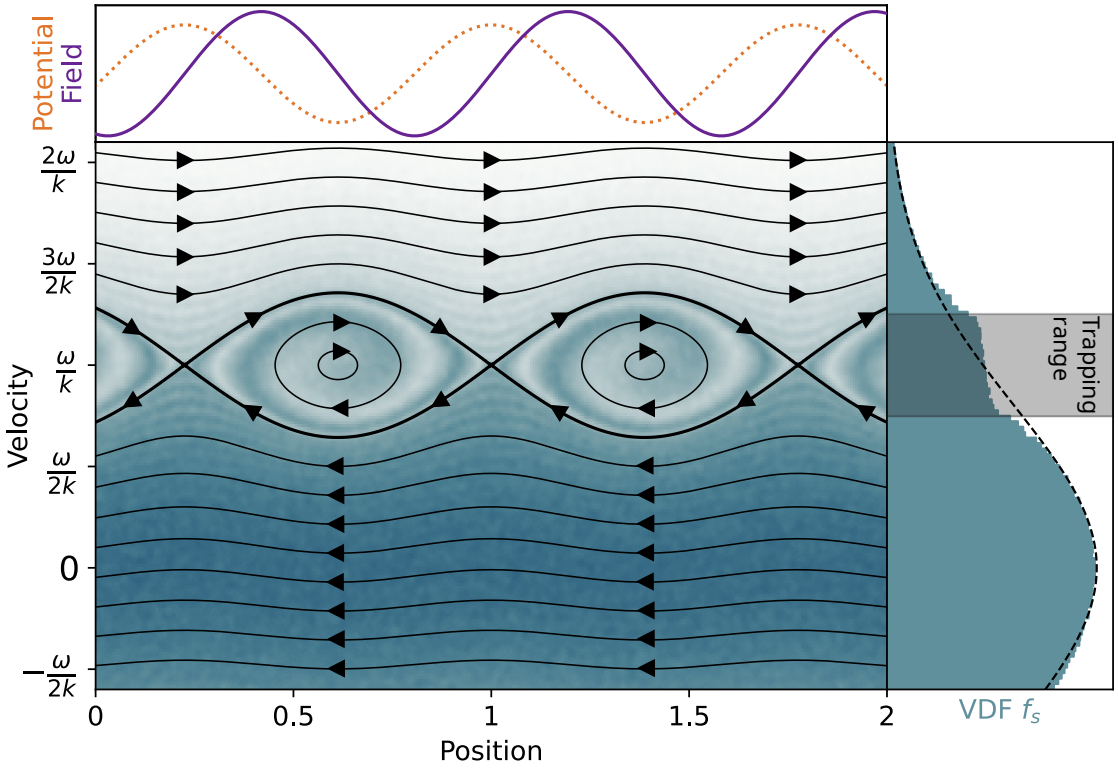

Figure 2.1: An overview of the phase space in the presence of an electrostatic wave with phase velocity $v_{\mathrm{ph}} = \omega/k$. The spatial variation of the electric field E (solid purple) and the electric potential ϕ (dotted orange) of the wave are displayed in the upper subplot. The centre subplot shows the full phase space, where darker colours indicate a higher phase space density. The solid lines with arrows indicate representative particle trajectories in the frame of reference where the wave is stationary (travelling with $v_{\mathrm{ph}} = \omega/k$). Notice the thick solid line which separates trapped and untrapped trajectories. The right subplot shows the velocity distribution function (VDF) after the Landau resonance (filled blue) and the initial VDF (dashed black). This figure is based on the work of Kunimune, 2023.

for $f_s' > 0$), as this corresponds to there being more particles depositing energy into the perturbations. Analogously, the perturbations decay where the gradient is negative (Landau damping for $f_s' < 0$), as this corresponds to more particles extracting energy from the perturbations. Through the interaction of the wave with the surrounding particles, the Landau resonance usually leads to a plateau around the resonance frequency ω_r of the wave (Kennel et al., 1966). The plateau formation is illustrated in the right subplot of fig. 2.1.

In this work, we choose to simply present the key results from linear theory instead of going through a full mathematical derivation, which can be found in kinetic plasma physics textbooks such as Swanson, 2003. The resonance condition in the linear theory is determined via the wave's frequency ω_r and wavenumber $\boldsymbol{k}$. It reads (Swanson, 2003):

$$\boldsymbol{k} \cdot \boldsymbol{v} = \omega_r. \tag{2.10}$$

Furthermore, we can quantify the growth or decay of the wave via the growth rate γ. Calculating γ analytically for the general case is difficult. The classic example is the one mentioned in section 2.1.1, namely plasma oscillations in an unmagnetized plasma. In that case (in the limit $|\gamma| \ll \omega_r$), γ can be calculated as (Swanson, 2003)

$$\gamma = \omega_r \frac{\pi \omega_{\mathrm{pe}}^2}{2k^2} \frac{d}{dv} F_{\mathrm{e}0}(v_{\mathrm{ph}}), \tag{2.11}$$

where $F_{\mathrm{e}0}$ is the marginal electron distribution in the direction of $\boldsymbol{v}_{\mathrm{ph}}$. It is normalized as $\int dv_{\parallel} F_{\mathrm{e}0} = 1$. The key insight from this example is that $\gamma \propto f'_{\mathrm{e}0}(v_{\mathrm{ph}})$. Finally, the (electron) trapping region is a velocity range that can be estimated via the electric potential ϕ:

$$v = v_{\mathrm{ph}} \pm \sqrt{\frac{2q_{\mathrm{e}}\phi}{m_{\mathrm{e}}}} \tag{2.12}$$

Note that ϕ is a function of position and time, which means that the size of the trapping region will change over time. We can also see that the trapping region for a species s depends on the charge-to-mass ratio q_s/m_s of the particle species.

2.2 Proton-alpha instability

The solar wind is a dynamically changing plasma stream that is emitted by the Sun (Neugebauer et al., 1966; Owens, 2020). It fills the entire heliosphere and spreads throughout the solar system, dragging with it the Sun's magnetic field (Neugebauer et al., 1966; Parker, 1958). In this stream, the density varies significantly over space and time (Lalti et al., 2022). On the other hand, all particle species in the same region always travel with roughly the same velocity (Owens, 2020).

The solar wind plasma at a distance of 1 AU (from the sun) mostly travels with super-Alvénic speeds which also makes it supersonic (Merka et al., 2005). However, near the Earth it comes in contact with the planet's magnetic field, which acts as an obstacle (Merka et al., 2005). Now, there is a critical boundary where the bulk speed abruptly drops from super-Alvénic to sub-Alvénic speeds and shock waves develop (Merka et al., 2005). This region is known as the bow shock. A sketch of its flow geometry is displayed in fig. 2.2. At the bow shock, a fraction of the solar wind particles is reflected while the remaining particles travel further downstream into the magnetosheath (Cohen et al., 2019). It is important to remember that the geometry of the bow shock and magnetosheath depend strongly on the properties of the incoming solar wind. Consequently, they change dynamically over time.

The proton-alpha instability is a streaming instability that was observed just downstream of the Earth's bow shock (Graham et al., 2024). The goal of this section is to understand why and under which conditions it forms. Furthermore, we want to understand how its dynamics change with the plasma parameters by using a simplified theoretical approach.

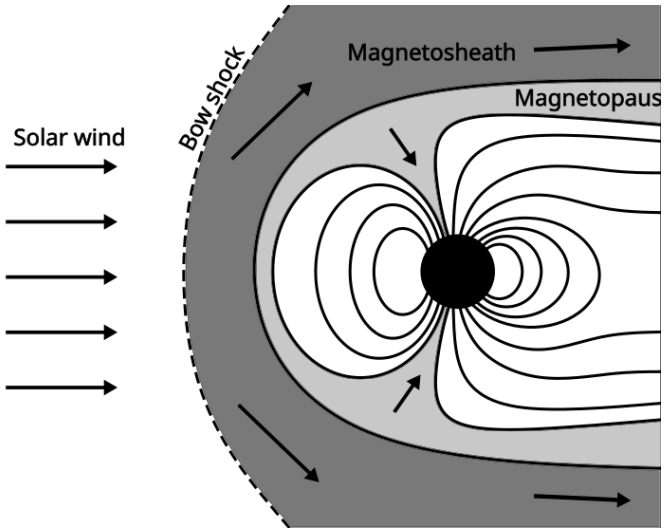

Figure 2.2: Illustration of the path of solar wind around the earth. The bow shock (dashed line), the magnetosheath (dark gray), and the magnetopause (border between light grey and white region) are distinguished by the behaviour of the flowing plasma.

2.2.1 Origin of the phenomenon

To understand the origin of the proton-alpha instability, we want to focus on the region near the bow shock. The deceleration across the bow shock depends on the charge-to-mass ratio q_s/m_s of the particle species. The larger gyro radius of the ions compared to electrons entails that incoming solar wind ions penetrate deeper into the magnetosheath than the electrons during their gyration. This causes a charge separation which yields an electrostatic cross-shock potential ϕ. The resulting force will act to restore the charge neutrality, by repelling ions and attracting electrons (Cohen et al., 2019).

As an approximation, we consider the shock ramp to be a step function. In this case, the difference between the upstream and downstream velocities $u_{s,\mathrm{u}}$ and $u_{s,\mathrm{d}}$ due to ϕ, is given by (Graham et al., 2025):

$$u_{s,\mathrm{u}}^2 - u_{s,\mathrm{d}}^2 = \frac{2q_s\phi}{m_s}. \tag{2.13}$$

It is clear that, in this simplified scenario, alpha particles will decelerate less than protons. This is in agreement with observations analysed by Graham et al., 2024. For a cross-shock potential of $\phi \approx 1200\,\mathrm{V}$, the flow velocity Δu_{d} between alpha particles and protons downstream of the shock reaches approximately $100\,\mathrm{km/s} - 200\,\mathrm{km/s}$ (Graham et al., 2025). Some fraction of the particle species, depending on the parameters of the shock, will be reflected (Kennel et al., 2013; Paschmann et al., 1980).

Particle species	n_s (1/cm^3)	T_s (eV)	u_s (km/s)
Electrons	12	100	0
Protons	10	12	0
Alphas	1	3	100

Table 2.1: The nominal plasma conditions used for this work are identical to those of Graham et al., 2025. The background magnetic field is zero.

2.2.2 Linear theory

This section outlines the derivation of the linear theory presented by Graham et al., 2025. The fundamental idea is to use the electrostatic dispersion relation of an unmagnetized, homogeneous plasma and was first presented by Gary, 1979. This linear dispersion relation can be derived in two steps. First, the distribution function $f_s(\boldsymbol{x}, \boldsymbol{v}, t)$ is expanded to first order around a spatial homogeneous steady state. The velocity distribution is assumed to follow a Maxwell-Boltzmann distribution $f_s^{(0)}(\boldsymbol{v})$ with flow speed $\boldsymbol{u}_s$. Secondly, the Vlasov equation in combination with the Poisson equation are solved for this linear ansatz (Gary, 1979). Finally, we make the assumption of a vanishing background magnetic field $\boldsymbol{B} = 0$. We will later test the validity of this assumption in section 4.5. Now, the dispersion relation can be written as (Gary, 1979):

$$0 = 1 - \frac{\omega_{\mathrm{pe}}^2}{k^2 v_{\mathrm{te}}^2} \mathcal{Z}' \left(\frac{\omega}{k v_{\mathrm{te}}} \right) - \frac{\omega_{\mathrm{pp}}^2}{k^2 v_{\mathrm{tp}}^2} \mathcal{Z}' \left(\frac{\omega}{k v_{\mathrm{tp}}} \right) - \frac{\omega_{\mathrm{p}\alpha}^2}{k^2 v_{\mathrm{t}\alpha}^2} \mathcal{Z}' \left(\frac{\omega - k_\parallel u_\alpha}{k v_{\mathrm{t}\alpha}} \right). \tag{2.14}$$

Here, $k_\parallel$ is the wavenumber parallel to the flow speed u_s. When the growth rate $\mathrm{Im}(\omega) = \gamma$ is positive, the Maxwellian equilibrium is an unstable fixed point. Here, waves can exponentially grow under Landau resonance (cf. section 2.1.2). Graham et al., 2025 numerically explores the parameter dependencies of this instability. As our baseline, we choose the same nominal plasma conditions as Graham et al., 2025 which are given in table 2.1. The flow speed of the alpha particles is in the x-direction, i.e. $\boldsymbol{u}_\alpha \cdot \hat{\boldsymbol{e}}_x = u_\alpha$.

In this work, we want to focus on the dependence of the wave properties (incl. growth rate) on the density ratio n_α/n_{p} and the flow speed u_α at the maximum growth rate $\gamma \to \gamma_{\max}$. This additional constraint on eq. (2.14) yields a unique solution for fixed plasma parameters. We denote the wave properties of the fastest growing wave, i.e. the wave with $\gamma_{\max} = \max(\gamma)$, using the subscript "max". For example, the wavenumber of the fastest growing wave is $k_{\max} \neq \max(k)$. Figure 2.3 displays the wave's properties under otherwise nominal conditions. A variation of the density ratio in fig. 2.3 (a) shows that instability occurs when $n_\alpha/n_{\mathrm{p}} > 10^{-3}$. The growth rate $\gamma_{\max}$ increases until it reaches a maximum at $n_\alpha/n_{\mathrm{p}} = 0.5$ where the charge density of protons and alphas is equal. Above $n_\alpha/n_{\mathrm{p}} \approx 2.5 \cdot 10^{-3}$, $\omega_{\max}/\omega_{\mathrm{pp}}$ increases as the fraction of alpha particles increases. The normalized wavenumber $k_{\max}\lambda_{\mathrm{D}}$ shows a local maximum at $n_\alpha/n_{\mathrm{p}} \approx 0.3$. Both $\omega_{\max}/\omega_{\mathrm{pp}}$ and $k_{\max}\lambda_{\mathrm{D}}$ change gradually with the density ratio. The phase speed v_{ph} monotonically decreases as n_α/n_{p} increases.

Figure 2.3 (b) displays the wave properties under a changing flow speed u_α. We

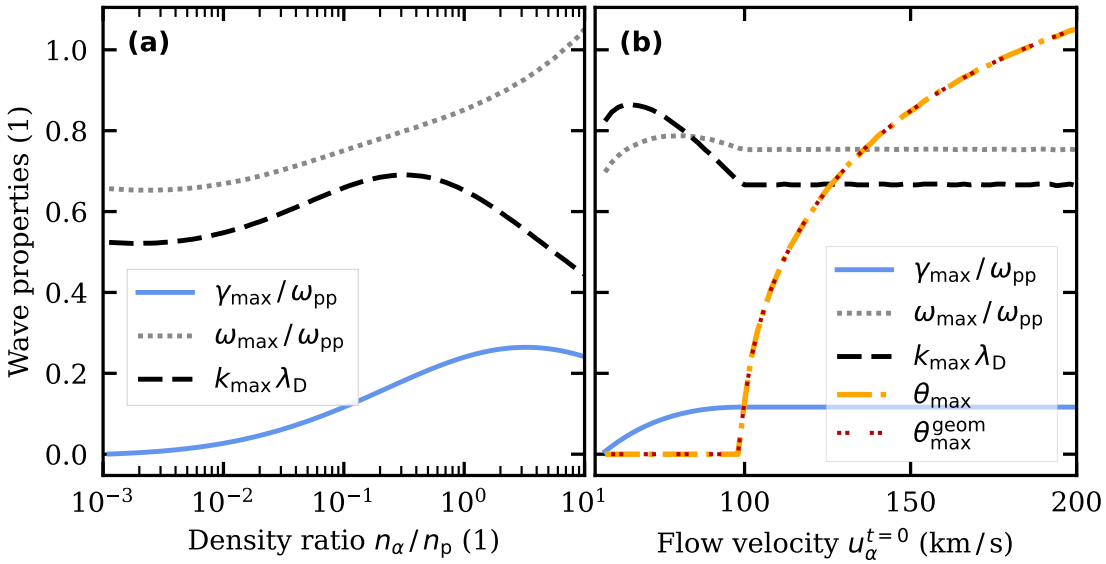

Figure 2.3: The predictions from the linear theory for growth rate γ_{max}, frequency ω_{max}, wavenumber k_{max}, and wave angle θ_{max} to the drift direction are under otherwise nominal conditions, based on the work of Graham et al., 2025. Fig. **(a)** varies the density ratio between protons and alpha particles such that $n_e = 12/cm^3 = n_p + 2n_\alpha$. Fig. **(b)** varies the alpha flow speed. The wave angle θ is in radians. For reference, the maximum angle is at $\theta_{max} \approx 60°$. Additionally, we show θ^{geom}_{max} which is calculated from eq. (2.15).

can see that the growth rate γ_{max}, wavenumber k_{max} and frequency ω_{max} only change for flow velocities below $u_\alpha \approx 98\,km/s$. The growth rate decreases monotonically until it approaches zero at $u_\alpha \approx 60\,km/s$. Figure 2.3 (b) also shows how the wave angle—i.e., the angle between $\boldsymbol{v}_{ph}$ and $\boldsymbol{u}_\alpha$, denoted by θ_{max}—changes with the flow speed u_α. This is the most interesting aspect and helps us understand the geometry of the instability in velocity or momentum space.

We can reason about the angular dependence $\theta_{max}(u_\alpha, k_{max}, \omega_{max})$ using the geometric considerations illustrated in fig. 2.4. Firstly, the developing wave has characteristic phase velocity $\boldsymbol{v}_{ph}$. This means that the interaction lies tangential to a circle around the origin with a radius v_{ph} (black, dotted in fig. 2.4). Additionally, from Landau resonance theory, we assume that the growth rate of a Landau resonant wave depends on the gradients $\nabla_v f_s$ (Swanson, 2003). Then, for a Maxwellian VDF, the fastest growing wave is located on some circle in velocity space with radius $v_{r\alpha}$ around the mean u_α (blue, dash-dotted in fig. 2.4). There, it should be maximal in the direction of v_{ph}. Both circles together fully constrain the location of the interaction to the dashed lines shown in fig. 2.4. The geometrical prediction of the angle $\theta^{geom}_{max} \equiv \theta_{max}$ is now given by

$$\theta^{geom}_{max} = \begin{cases} \arccos\left(\frac{v_{ph}+v_{r\alpha}}{u_\alpha}\right) & u_\alpha > v_{ph} + v_{r\alpha} \\ 0 & u_\alpha \leq v_{ph} + v_{r\alpha} \end{cases}. \tag{2.15}$$

In the numerical scheme which solves eq. (2.14), we can search for γ_{max} over all

possible k, ω, and θ. Subsequently, we use $k_{\max}$, $\omega_{\max}$ to calculate v_{ph} for a given u_α. Finally, we determine $v_{\mathrm{r}\alpha} \approx 1.3 v_{\mathrm{t}\alpha} \approx 30\,\mathrm{km/s}$ via a fit to $\theta_{\max}$. Figure 2.3 (b) shows a direct comparison of eq. (2.15) (denoted $\theta_{\max}^{\mathrm{geom}}$) with the solution of the dispersion relation (denoted $\theta_{\max}$). We find an exact match ($\theta_{\max}^{\mathrm{geom}} = \theta_{\max}$) up to the resolution limit of the numerical scheme. This confirms the validity of our geometrical interpretation. Figure 2.4 also gives an intuition about the change in $k_{\max}$ and $\omega_{\max}$ in regime where $u_\alpha < v_{\mathrm{ph}} + v_{\mathrm{r}\alpha}$. This is because there are no internal bitangent lines when the phase speed $v_{\mathrm{ph}} = \omega_{\max}/k_{\max}$ and $v_{\mathrm{r}\alpha}$ stay constant. Now, $v_{\mathrm{r}\alpha}$ does not depend on u_α and the radius of the circle around $\boldsymbol{u}_\alpha$ cannot change. Instead, a decrease of v_{ph} to $v_{\mathrm{ph}} = \omega_{\max}/k_{\max} \leq u_\alpha - v_{\mathrm{r}\alpha}$ is necessary. Finally, wave growth is no longer possible when $v_{\mathrm{ph}} \approx 60\,\mathrm{km/s}$.

Notably, the linear Landau resonance theory of plasma oscillations suggests that the fastest growing waves should be located at the maximum gradient:

$$\max_v(\|\nabla_v f_\alpha\|) = v_{\mathrm{t}\alpha}/\sqrt{2} \approx 17\,\mathrm{km/s}.$$

However, this is in disagreement with the result from the linear dispersion relation $v_{\mathrm{r}\alpha} \approx 30\,\mathrm{km/s}$, where waves preferably grow at more shallow gradients of f_α. One possible reason for this difference is that, unlike the plasma oscillation, the instability considered here interacts with multiple species simultaneously.

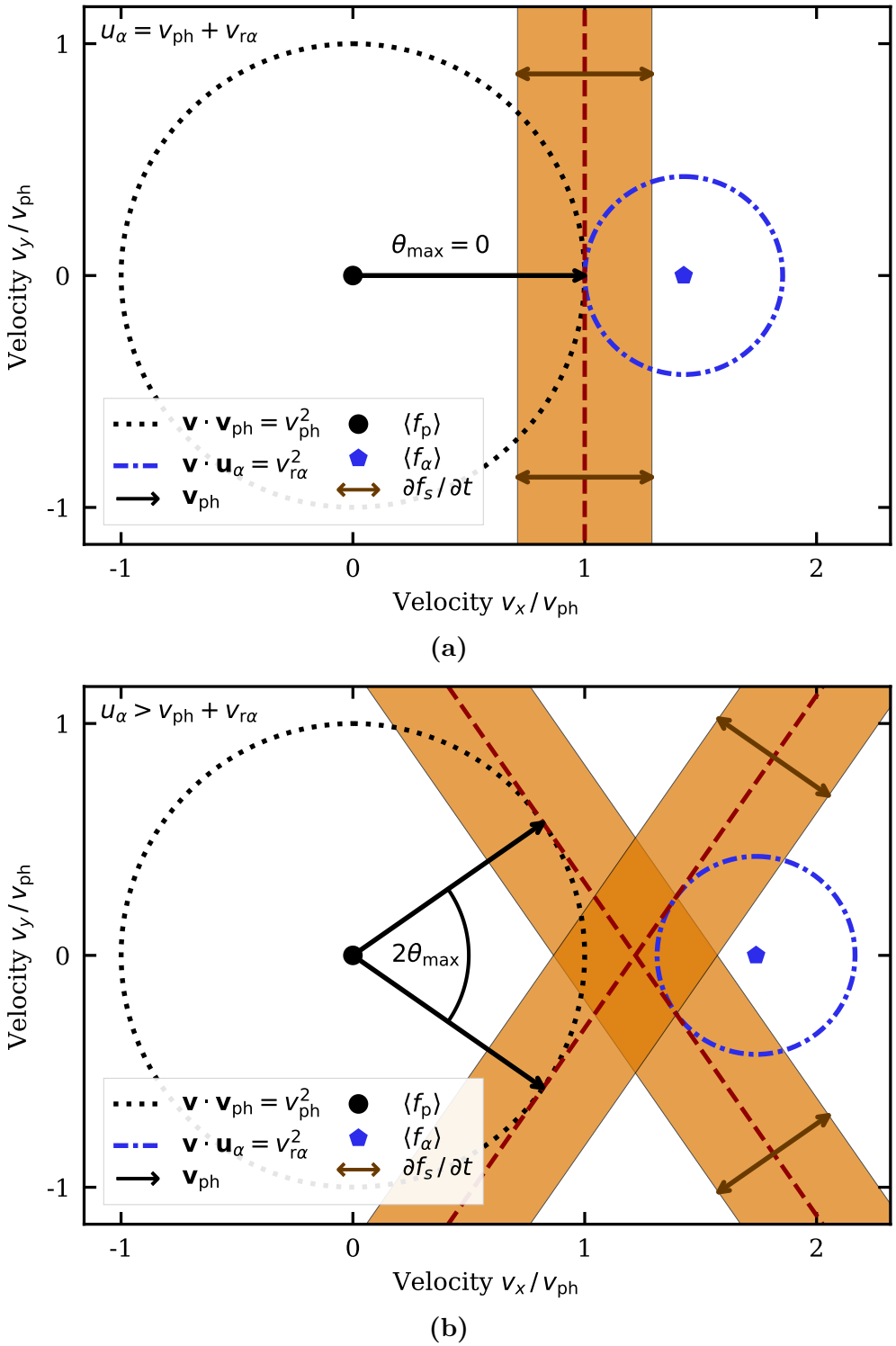

Figure 2.4: Illustration of the dynamics and geometry in velocity space depending on the alpha flow velocity. The mirror symmetry around $v_y = 0$ reflects the rotational symmetry of the phase space around the x-axis. The width of the trapping range (dark orange bands) changes over time and is chosen only for illustration purposes. The arrows in the trapping range indicate the direction of particle displacement by the wave. Fig. **(a)** shows $u_\alpha = v_{ph} + v_{r\alpha}$ with wave angle $\theta_{max} = 0$. Fig. **(b)** shows $u_\alpha > v_{ph} + v_{r\alpha}$ with wave angle $\theta_{max} > 0$.

3

The Particle-In-Cell plasma simulation method

In the following, we briefly describe the numerical methods used to solve the plasma dynamics. Self-consistent plasma modelling is generally done either via fluid, kinetic, or hybrid descriptions (Dijk et al., 2009).

Fluid codes assume that each particle species forms a continuous medium. The individual particles are not simulated, and the dynamics are reduced from the full distribution function of the system to its first few (velocity integral) moments (Davidson, 2001; Dijk et al., 2009). For example, the simplest form of magnetohydrodynamics models the plasma only via a single centre-of-mass velocity and current density that combines the bulk velocities u_s, number densities n_s, charges q_s, and masses m_s of all species. The system of equations is then closed by evolving the temperature T_s by a chosen equation of state (Davidson, 2001). These simplifications can only be rigorously justified for a sufficiently collisional plasma, which is often not a satisfactory model for essentially collisionless space plasmas environments (Freidberg, 2014). Thus, many physical effects and phenomena cannot be explained using such fluid models (Birdsall et al., 2018; Davidson, 2001; Dijk et al., 2009).

In this work, the fully kinetic Particle-In-Cell (PIC) code called EPOCH is used (Arber et al., 2015). Here, the full distribution function of the Vlasov-Maxwell equations are solved indirectly through a Lagrangian approach (Arber et al., 2015; Birdsall et al., 2018). This means that EPOCH simulates particle trajectories. At the same time, the electric and magnetic fields are calculated on a discrete spatial grid through interpolation (Arber et al., 2015; Birdsall et al., 2018). In contrast to the fluid modelling approach, PIC simulations only neglect direct particle-particle interactions and estimate the full distribution functions[1]. For our setup, this is well justified because the mean free path l is roughly $l = 4 \cdot 10^5\,\mathrm{km}$ in the solar wind (Coburn et al., 2022). To illustrate, roughly one out of 10^5 particles is expected to collide once over the course of the entire simulation.

An overview of the calculations for particle motion and electromagnetic fields follows to obtain an intuition of the algorithm, which is implemented in the EPOCH code. We present the reasoning behind the choice for grid resolution and domain size. Finally, we discuss the numerical stability of the algorithms.

[1] In principle, EPOCH is able to simulate effects due to collisions, partial ionization, and other phenomena (Arber et al., 2015). These are not relevant for our simulation case.

3.1 Evolution of the plasma dynamics

EPOCH is a kinetic plasma code. This means that individual particles are simulated, as illustrated by the gray dots in fig. 3.1. However, it is computationally intractable to simulate all particles (Arber et al., 2015; Birdsall et al., 2018). Instead, pseudoparticles (or "macroparticles") representing many real particles have to be introduced. In this work, the ratio between real particles and pseudoparticles is on the order of 10^5. This description via pseudoparticles is convenient in a collisionless plasma, where the binary Coulomb interactions can be neglected. The particle dynamics are then determined by the Lorentz force, which only depends on the charge-to-mass ratio $q_s \,/\, m_s$ of the particle (cf. eq. (1.1)). This ratio is the same for real particles and pseudoparticles. The position $\boldsymbol{x}$ and momentum $\boldsymbol{p}$ of each pseudoparticle are evolved (Arber et al., 2015; Birdsall et al., 2018). The velocity $\boldsymbol{v}$ of the particle is then calculated via the Lorentz factor from the momentum $\boldsymbol{p}$. This enables a fully relativistic description (Arber et al., 2015). A modified version of the leapfrog integration method is used as the numerical algorithm (Arber et al., 2015).

The particle update via the Lorentz force (cf. eq. (1.1)) also requires the electric field $\boldsymbol{E}$ and magnetic field $\boldsymbol{B}$ at each particle position $\boldsymbol{x}$. Therefore, it is essential to correctly and efficiently solve Maxwell's equations. This is implemented using the Finite-difference time-domain method (Arber et al., 2015; Birdsall et al., 2018). Figure 3.1 illustrates this procedure. The electric field $\boldsymbol{E}$, magnetic field $\boldsymbol{B}$ and current $\boldsymbol{J}$ are calculated at discrete locations on a regular, spatial, Cartesian grid.

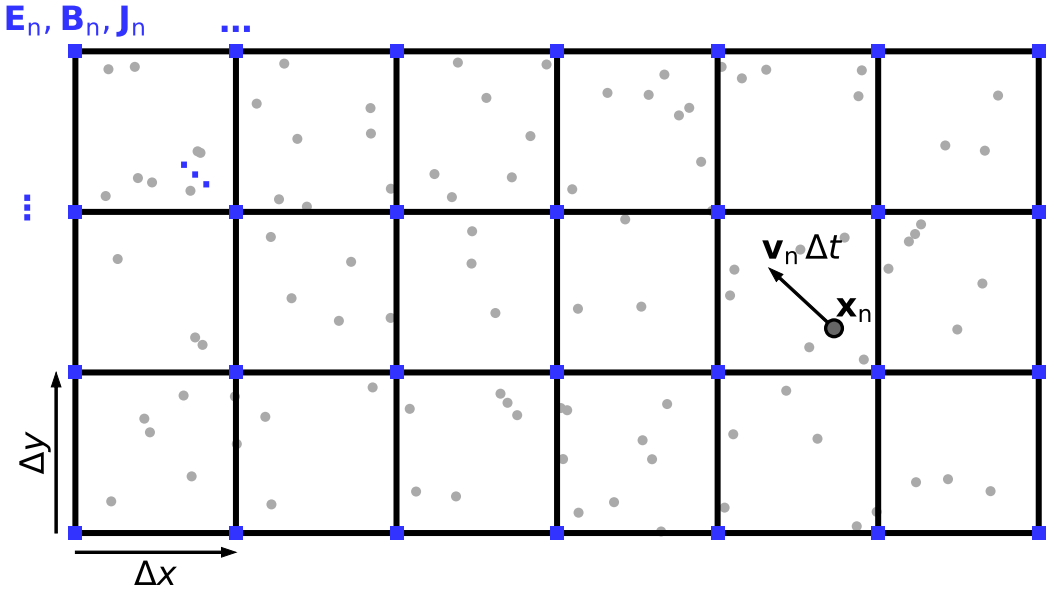

Figure 3.1: At timestep n, each particle has a position $\boldsymbol{x}_\mathrm{n}$ and velocity $\boldsymbol{v}_\mathrm{n}$. Currents $\boldsymbol{J}_\mathrm{n}$, electric fields $\boldsymbol{E}_\mathrm{n}$, and magnetic fields $\boldsymbol{B}_\mathrm{n}$ are calculated at discrete points on a regular Cartesian grid. Note that this illustration is a simplification from the actual calculations of Yee's method (Yee, 1966).

Their values are computed from the state of the nearby pseudoparticles, weighted by their distance (Arber et al., 2015; Birdsall et al., 2018; Yee, 1966). For example, the electric field $\boldsymbol{E}_{\mathrm{n}}^{(j,k)}$ at time step n and grid point with index (j, k) is determined via the charge density ρ. This charge density can be estimated by summing over the individual pseudoparticle charges. Each charge is weighted by a chosen shape function that depends on the distance of the particle to the grid point (j, k). Afterwards, the acting force from $\boldsymbol{E}_{\mathrm{n}}^{(j,k)}$ is interpolated back onto each nearby particle. This procedure produces a self-consistent solution to Maxwell's equations for a given grid size (Birdsall et al., 2018; Yee, 1966). Information on the fundamental principles of PIC simulations is available in Birdsall et al., 2018. Arber et al., 2015 discusses the concrete implementation in the EPOCH code.

3.2 Modelling constraints

It is important to understand that both the number of pseudoparticles and the grid resolution offer a trade-off between simulation quality and computational cost (Birdsall et al., 2018). Neither the total number of pseudoparticles N_{sim} nor the number of grid cells N_{cell} can be used as a measure of quality alone. Instead, we consider the number of pseudoparticles per cell $N_{\mathrm{sim}}/N_{\mathrm{cell}}$. This is because electromagnetic fields are calculated locally from the particle state in each cell (Birdsall et al., 2018; Yee, 1966). Additionally, the ratio $N_{\mathrm{sim}}/N_{\mathrm{cell}}$ also limits the smoothness of the distribution function $f_s(\boldsymbol{r}, \boldsymbol{v}, t)$ which, in turn, determines the accuracy of derived quantities like the bulk velocity $\boldsymbol{u}_s$ or the temperature T_s. Thus, the primary limitation becomes the grid resolution.

The simulation grid must be set up such that it resolves both the smallest and the largest spatial structures of interest (Birdsall et al., 2018). In our setup, we do not know these wavelengths beforehand. Thus, we must measure them. In our simulations, the boundary is period in all spatial directions. Thus, the k-space resolution $\Delta k = 2\pi/(\Delta x\, N_{\mathrm{cell,x}})$ places a strict constraint on the precision of our measurements. It depends only on the cell side length Δx and the number of cells $N_{\mathrm{cell,x}}$ in the x-direction. In particular, the periodicity of our simulation domain only allows the formation of waves with wavelength $\lambda = 2L/j$ where $j \in \mathbb{N}$ and L is the box's side length (Swanson, 2003). This effectively means that many wave lengths are forbidden unless we choose a large box size $L \gg \lambda$.

3.3 Numerical stability

The finite-difference time-domain (FDTD) scheme used by EPOCH is second-order accurate (Arber et al., 2015). This means that the error ϵ scales quadratically with the grid sizes Δx and Δy. In other words, for $\Delta x = \Delta y$ the error follows $\epsilon \propto \Delta x^2$. Additionally, the leapfrog integration method is time-reversible, meaning that one arrives back at the starting values when integrating forward and backward the same number of steps[2]. Finally, leapfrog integration conserves the energy of any

[2]This statement discards errors due to limited precision with floating-point numbers.

Hamiltonian system like our setup.

While the symplectic nature of the leapfrog method provides conservation of energy to the numerical scheme, this alone is not sufficient. The time step size is bounded by the Courant-Friedrichs-Lewy (CFL) condition (Courant et al., 1928):

$$\Delta t_{\text{sim}} \leq \left(\frac{c^2}{\Delta x^2} + \frac{c^2}{\Delta y^2} + \frac{c^2}{\Delta z^2} \right)^{-\frac{1}{2}}. \tag{3.1}$$

An intuitive way to understand the CFL condition is that all information is constrained to move less than one grid cell per time step.

4

Results

In this chapter, we present and discuss our results obtained from PIC simulations of the proton-alpha instability. Section 4.1 covers the non-linear evolution of the instability. Additionally, it introduces different representations and metrics to characterize the plasma dynamics through the simulation data. Afterwards, the majority of this chapter deals with parameter variations over the density ratio n_α/n_p, alpha flow speed u_α, as well as the direction and strength of the background magnetic field $\boldsymbol{B}_0$. Here, we aim to understand how the plasma heating and the wave properties change at different plasma parameters.

As discussed in section 3.2, the correct choice of simulation parameters is crucial to ensure accurate results. From the linear theory in section 2.2.2, it is clear that $k\lambda_\mathrm{D} \approx 1$ for most cases. Therefore, we choose $\Delta x = \Delta y = \lambda_\mathrm{D}/2$ for all simulations. For the variations over u_α and $\boldsymbol{B}_0$, we perform two-dimensional simulations with 128 grid cells in the x-direction (aligned with the drift), and at least 64 grid cells in the y-direction, depending on the wave angle. For the variation of n_α/n_p, we perform the one-dimensional simulations with twice the domain size at the same resolution (256 grid cells). In section 4.2, we vary the number of pseudoparticles per cell $N_\mathrm{sim}/N_\mathrm{cell}$ and find that $N_\mathrm{sim}/N_\mathrm{cell} = 2^{10}$ are sufficient for accurate simulation at a reasonable computational cost. Across all simulations, the domain has periodic spatial boundary conditions.

4.1 Evolution of the instability

The instability and its evolution can in large parts be characterized through the electrostatic waves which develop. Figure 4.1 shows the electric field E_x and its mean electric field energy $\langle W_E \rangle_x$ over time through a one-dimensional simulation. Here, we use this representation primarily to explain the different phases of the temporal evolution.

Initially, up to $t\,\omega_\mathrm{pp} \approx 20$, the electric field energy (solid black) in fig. 4.1 (b) fluctuates around $\langle W_E \rangle_x \approx 3 \cdot 10^4$. This reflects the fundamental discretization noise in the simulation due to the finite number of particles, and we expect $\lim_{N_\mathrm{sim}\to\infty} W_E^{t=0} = 0$. Note however that this limit does not correspond to reality, where we also have a finite number of particles[1]. In fact, a certain level of initial

[1]This limit is comparable to a continuum simulation. It can represent the initial Maxwell-

noise is needed. These non-uniform particle movements correspond to a perturbation of the charge density and therefore also of the electric field. Now, a range of modes within this random perturbation grow exponentially, as predicted by the Landau theory (cf. section 2.1.2). However, it only surpasses the noise level after $t\,\omega_{\mathrm{pp}} \approx 20$ where it becomes visible in fig. 4.1.

Around $t\,\omega_{\mathrm{pp}} = 40$, the electric field energy caused by the growing wave far exceeds the energy of the noise such that $\langle W_E \rangle_x \gg \langle W_E^{t=0} \rangle_x$. From this point, the total electric field energy grows exponentially up to $t\,\omega_{\mathrm{pp}} \approx 50$ in fig. 4.1 (b). Due to the logarithmic scaling $\ln(\langle W_E \rangle_x) \propto t$ on the axis, this appears as the linear regime (thick orange), with an average slope of 2γ (dashed blue). Meanwhile, fig. 4.1 (a) also spatially resolves the phenomenon. It becomes clear that waves grow from small perturbations in the electric field. These emerge because of the inhomogenous way in which the pseudoparticles move throughout the simulation domain. Consequently, against the assumption in the Landau resonance theory of section 2.1.2, the wave onset is also spatially inhomogeneous. The angle of the blue and red bands in this regime of fig. 4.1 (a) represents the collective movement of all crests and troughs of the wave with its dominant phase velocity v_{ph}.

Beyond $t\,\omega_{\mathrm{pp}} \approx 50$, we observe how multiple wave crests combine into one: The wavelength changes, and non-linear effects begin to influence the dynamics of the plasma. At the same time, the wave energy begins to deviate from its exponential scaling in fig. 4.1 (b). From this point onwards, the linear theory is no longer able to predict the dynamics as higher order effects become relevant. Finally, around $t\,\omega_{\mathrm{pp}} = 60$, the mean electric field energy $\langle W_E \rangle_x$ reaches its maximum and starts to slowly decrease over time. The clear separation into crests and troughs of a typical sinusoidal wave is replaced by more complex structures in fig. 4.1 (a).

Generally, the regime where the total electric field energy grows linearly is hard to define precisely. Here, in order to avoid data dredging, we implement the automated procedure illustrated in fig. 4.1 (b). First, we compute $\langle W_E \rangle_{\boldsymbol{r}}$ over the entire simulation time. Secondly, we fit a seventh order polynomial to that time series. The inflection point after (in time) the lowest extremum in the data range is used as the start of the linear regime. Finally, the linear regime ends when the slope of the polynomial deviates by more than 20 % from its value at the inflection point. While the technical details of this procedure are mostly arbitrary, we find that the result agrees with the visual intuition of most simulations in this work. The growth rate γ_{max} can be estimated from the slope over the linear regime, as illustrated in fig. 4.1 (b). We can also use the spatio-temporally resolved electric field to estimate k_{max} and ω_{max}. For the one-dimensional case, they are computed as:

$$k_{\mathrm{max}} = \mathrm{argmax}_k(\langle \mathcal{F}_x(E) \rangle_t) \tag{4.1}$$

$$\omega_{\mathrm{max}} = \mathrm{argmax}_\omega(\langle \mathcal{F}_t(E) \rangle_x), \tag{4.2}$$

where $\langle \cdot \rangle_{x,t}$ denotes averaging over the subscript parameter and $\mathrm{argmax}_{x,k}(\cdot)$ denotes the taking the value of the subscript parameter where $\cdot$ is maximal. Note that we

Boltzmann distribution exactly and replaces the discrete particles by a continuum.

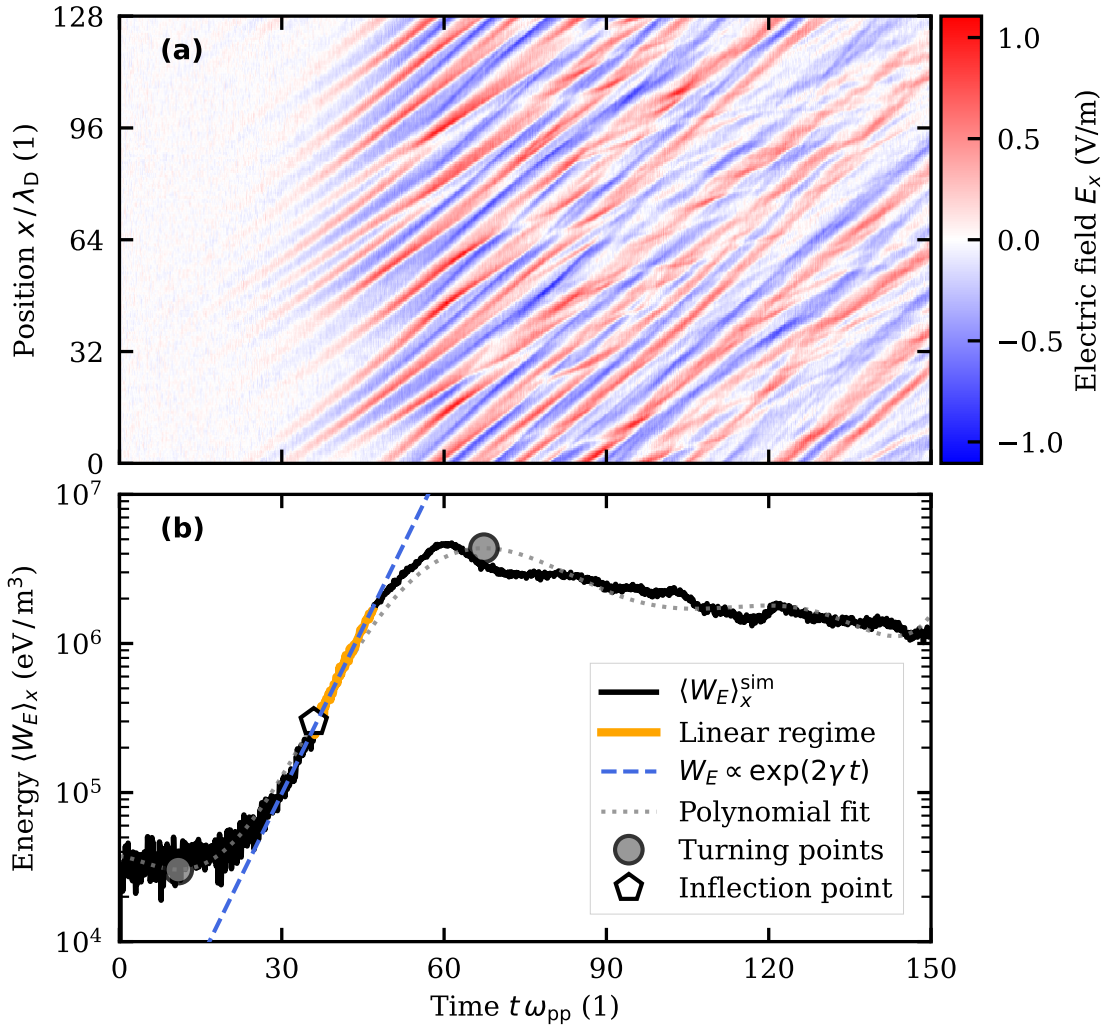

Figure 4.1: The spatio-temporal evolution of the instability in terms of **(a)** the electric field $E_x(x,t)$ and **(b)** its mean energy $\langle W_E(x,t) \rangle_x$ are shown here. Additionally, the method of identifying the linear growth phase and fitting the growth rate is illustrated in **(b)**. The data was captured in a one-dimensional simulation with $N_{sim} \,/\, N_{cell} = 2^{13}$ under nominal plasma conditions (cf. table 2.1).

only consider the time from the start of the simulation until the end of the linear regime, and that the discrete Fourier transform is used for $\mathcal{F}$.

The electron, proton, and alpha particle distribution functions in the simulations can be directly inferred from the pseudoparticles. They allow us to understand the particle dynamics of the different particle species. Additionally, we can compute the bulk velocities, temperatures, and higher-order moments of these distributions. Figure 4.2 covers the temporal evolution of the spatially averaged distribution functions, i.e. $\langle f_s(x,v,t) \rangle_x$. Note that due to the normalization, the apparent size of f_s is comparable across particle species. However, in absolute units, the distributions vary by orders of magnitude because of the differences in species densities (cf.

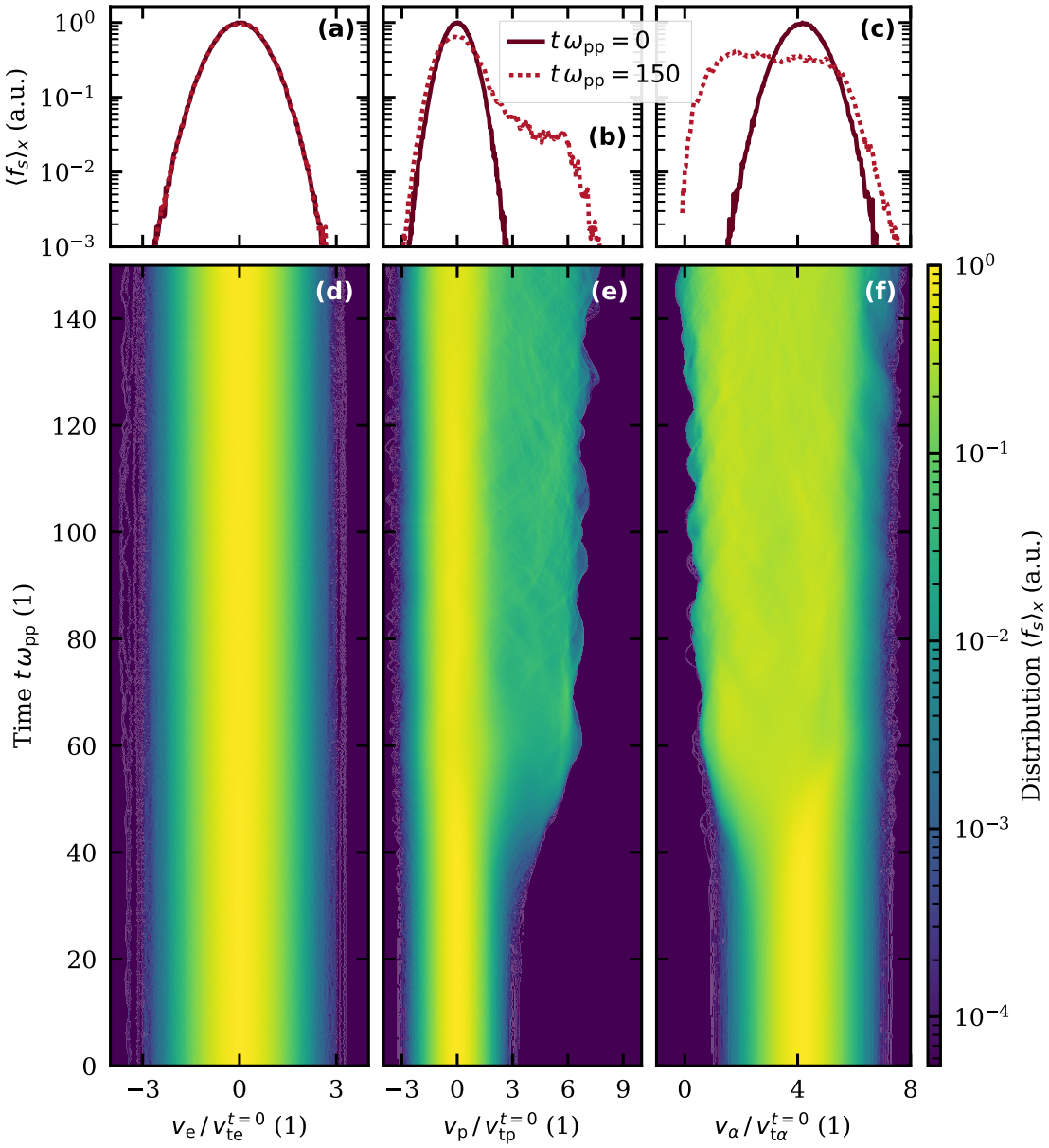

Figure 4.2: The temporal evolution of the distribution function $\langle f_s(x, v_x, t) \rangle_x$ for electrons, protons, and alpha particles going from left to right. All distributions are normalized such that their maximum at $t = 0$ is at unity. Subplots **(a)**, **(b)**, and **(c)** show the distribution functions at initial conditions and final simulation state, while subplots **(d)**, **(e)**, and **(f)** show the full evolution. The data was captured in a one-dimensional simulation with $N_{sim} / N_{cell} = 2^{13}$ under nominal plasma conditions (cf. table 2.1).

table 2.1) and $v_{\mathrm{te}} \gg v_{\mathrm{tp}} \approx v_{\mathrm{t}\alpha}$.

First and foremost, it is clear that the electron dynamics does not play an active role in the instability. Figure 4.2 (a) and (d) illustrate that the electron distribution functions remain Maxwellian throughout the entire simulation. This is because the electron thermal velocity v_{te} is much larger than the phase velocity $v_{\mathrm{ph}} \approx 0.01 v_{\mathrm{te}}$ of the growing waves. Thus, the Landau resonance takes place primarily in the centre of the distribution $v_{\mathrm{ph}} \pm v_{\mathrm{trap,e}} \approx (0.01 \pm 0.5) v_{\mathrm{te}}$. Here, the gradient f_{e}' is shallow, which means that f_{e} is already rather flat. The electron temperature T_e which characterizes the width of f_{e} increases only slightly by $\Delta T_e \approx 0.4\,\mathrm{eV} \ll T_e^{t=0} \approx 98.8\,\mathrm{eV}$. This heating takes place almost exclusively in the drift direction such that $\Delta T_{\mathrm{e},x} \approx 1.2\,\mathrm{eV} \approx 3\Delta T_e$.

On the other hand, the proton, and alpha particle distribution functions f_{p} and f_α significantly broaden over the simulation time. The largest visual changes in fig. 4.2 (e) and (f) happen around the linear growth phase from $t\,\omega_{\mathrm{pp}} \approx 30$ to $t\,\omega_{\mathrm{pp}} \approx 60$. We can see that f_{p} obtains an increasing number of high velocity particles in the drift direction ($v_{\mathrm{p}} \gg v_{\mathrm{tp}}^{t=0}$). Meanwhile, the alpha particles are slowing down to $v_\alpha \ll u_\alpha^{t=0} \approx 4 v_{\mathrm{t}\alpha}^{t=0}$. This reflects changes in the bulk velocities of $\Delta u_{\mathrm{p}} \approx 0.4 v_{\mathrm{tp}}^{t=0}$ and $\Delta u_\alpha \approx -v_{\mathrm{t}\alpha}^{t=0}$. Overall, this reflects the fact that both species approach their common flow velocity of approximately $2u_\alpha^{t=0}/7$ (for the density ratios in table 2.1). At the same time, we observe significant broadening of f_{p} and f_α. This entails an increase in temperatures by $\Delta T_{\mathrm{p},x} \approx 11\,\mathrm{eV}$ and $\Delta T_{\alpha,x} \approx 42\,\mathrm{eV}$ compared to $T_{\mathrm{p}}^{t=0} \approx 3\,\mathrm{eV}$ and $T_\alpha^{t=0} \approx 12\,\mathrm{eV}$. In summary, we can say that the alpha particles lose approximately 40 % of their directed kinetic energy ($\Delta K_\alpha \approx 0.4 K_\alpha^{t=0}$). This energy is primarily converted into plasma heating ($0.95\Delta K_\alpha$) which is split between alpha heating (50 %), proton heating (34%), and electron heating (16%). The remaining energy ($0.05\Delta K_\alpha$) is converted primarily into kinetic energy of the protons along the drift direction ($> 99\%$).

Figure 4.2 (c) shows that f_α develops a wide, flat centre as its average flow velocity decreases. The final width and centre of the flattop at $t\,\omega_{\mathrm{pp}} = 150$ is comparable to the trapping range $2.9 v_{\mathrm{t}\alpha} \pm 2 v_{\mathrm{t}\alpha}$ predicted from linear Landau theory (cf. section 2.1.2). The proton distribution f_{p} is also vastly affected (cf. fig. 4.2 (b)). The trapping range is located at approximately $2.9 v_{\mathrm{tp}} \pm 2.7 v_{\mathrm{tp}}$. The key difference here is that the entire alpha particle distribution is captured and flattened by the Landau resonance, whereas for the protons, the interaction range does not reach the centre of the distribution at $u_{\mathrm{p}} = 0$ and is instead shifted towards higher velocities.

Figure 4.3 complements fig. 4.2 by the explicit temporal evolution of the (three-dimensional) temperature T_s and $T_{s,x}$, the temperature in the drift direction. The measurement of the three-dimensional temperature is possible because EPOCH always simulates particle velocities in three dimensions, even when the spatial dimensionality is reduced (cf. section 3.1). In particular, fig. 4.3 highlights that the majority of the plasma heating for all particle species takes place during the linear growth phase. Additionally, we observe that the heating of all particle species is dominated by heating in the x-direction ($\Delta T_{s,x} \approx 3\Delta T_s$).

Finally, we want to gain an understanding of the full position-velocity phase

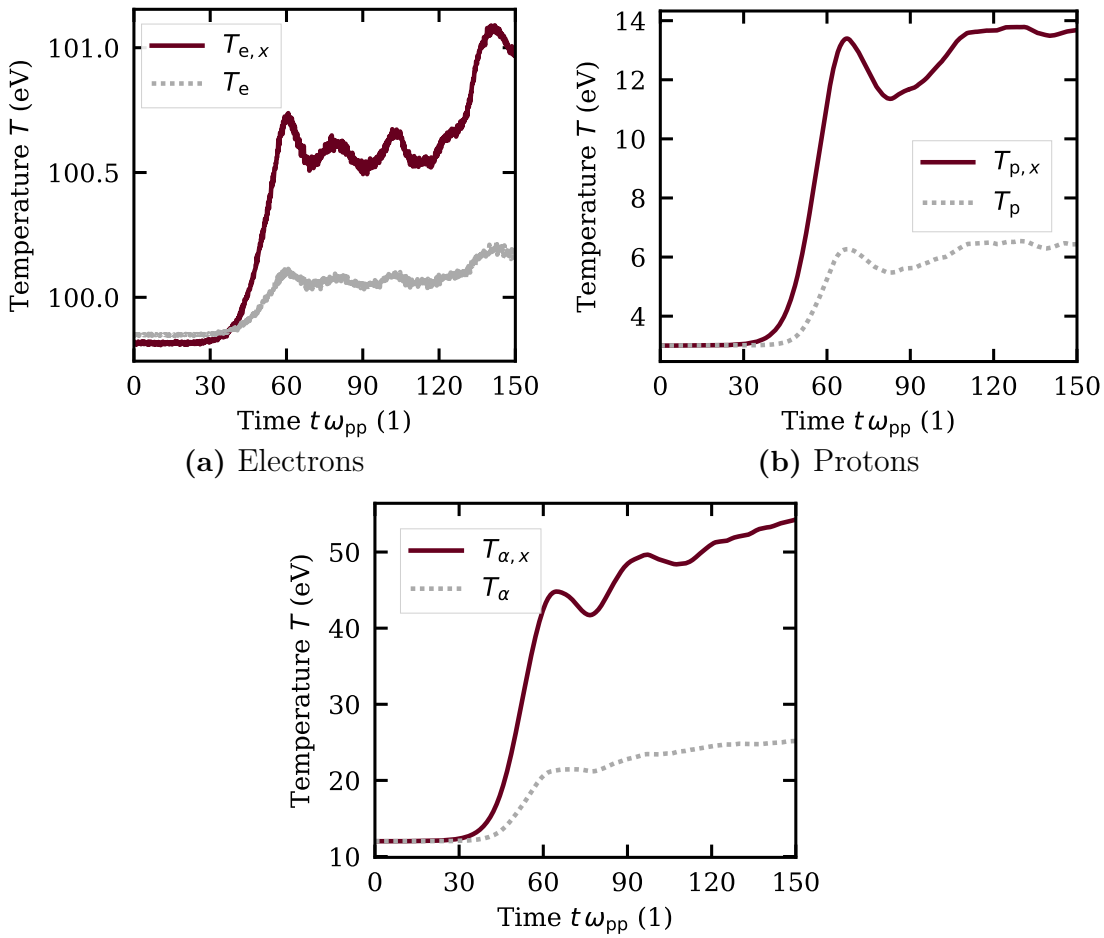

(a) Electrons **(b)** Protons

(c) Alpha particles

Figure 4.3: This figure shows the temporal evolution of the mean temperatures $\langle T_s(x,t)\rangle_x$ for all species. The solid lines represent three-dimensional temperatures, while dotted lines indicate temperatures in the x-direction. The data was captured in a one-dimensional simulation with $N_{\text{sim}} / N_{\text{cell}} = 2^{13}$ under nominal plasma conditions (cf. table 2.1).

space of the particle distribution functions. Figure 4.4 displays three snapshots at initial conditions $t\,\omega_{\text{pp}} = 0$, after the linear growth phase at $t\,\omega_{\text{pp}} = 60$, and after the full simulation period at $t\,\omega_{\text{pp}} = 150$ for the protons and alpha particles. The spatial component of the electrons is omitted, as it does not undergo any visible changes over the time span of the simulation.

Initially, both f_α and f_{p} follow a Maxwell-Boltzmann distribution and are spatially homogeneous up to the discretization noise of the pseudoparticles. This noise represents the perturbation necessary for the waves of the instability to grow. As the amplitude of electrostatic waves grows, phase space holes form due to the periodic potential landscape in x. These holes we observe in fig. 4.4 (a) and (b) are very comparable to those in fig. 2.1. However, the magnitude of the electric field in our simulations is much larger than that of fig. 2.1. Consequently, the separatrix of the wave is no longer surrounded by particles on both sides, and we observe the formation of these asymmetric arm-like structures where particles are accelerated

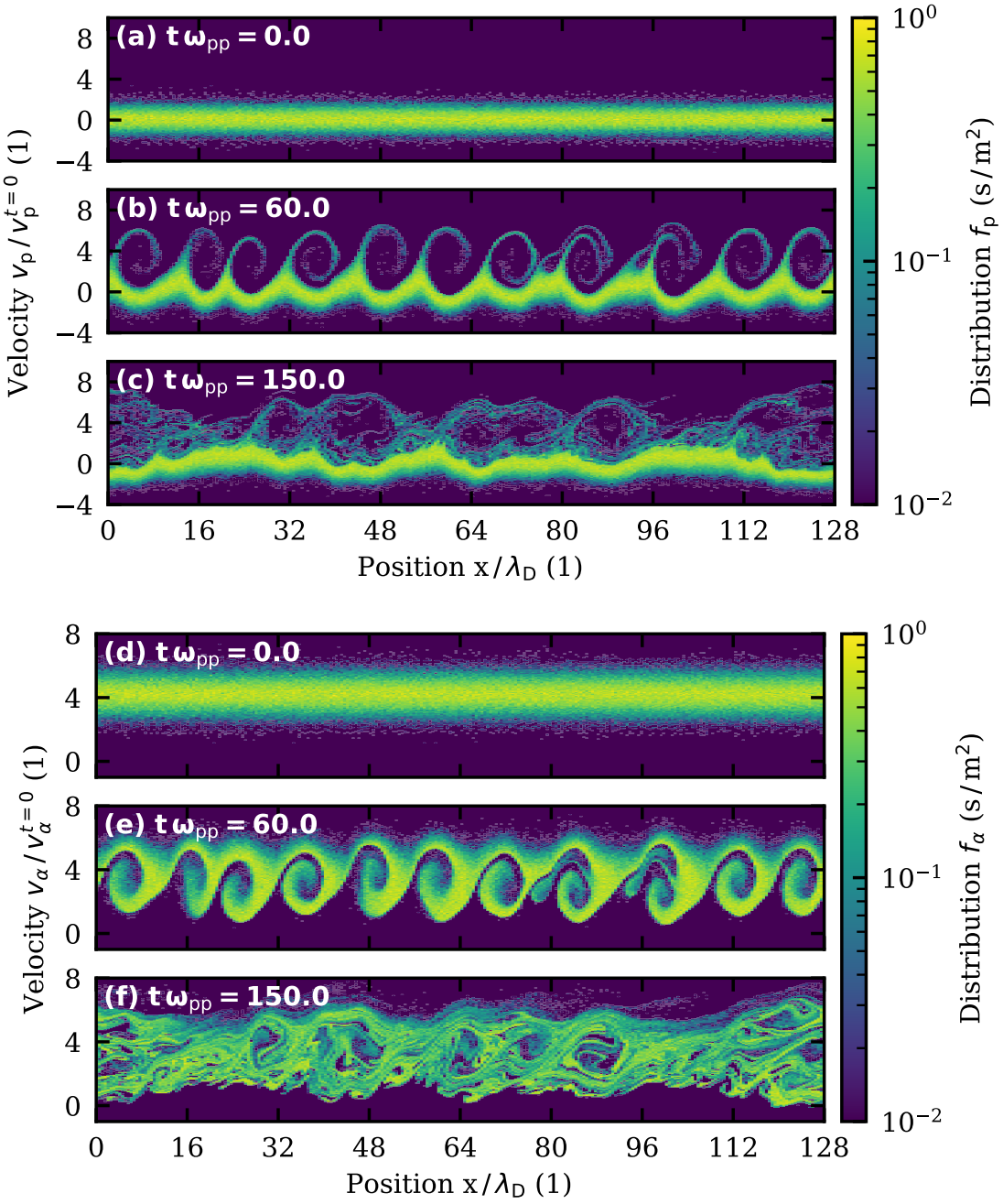

Figure 4.4: This figure shows the spatial structure of the distribution function $f_s(x, v_x, t)$ for the initial state, the state after the linear growth phase, and the final simulation state. Subplots **(a)** and **(b)** show distribution functions for protons and alpha particles normalized to a maximum at unity. The data was captured in a one-dimensional simulation with $N_{\text{sim}} \,/\, N_{\text{cell}} = 2^{12}$ under nominal plasma conditions (cf. table 2.1).

to high or decelerated to low velocities, respectively. The first non-linear effects are visible around the two phase space holes near $x/\lambda_\mathrm{D} = 85$ and $x/\lambda_\mathrm{D} = 100$, where the structures split into multiple bands. Finally, at the end of the simulation time at $t\,\omega_\mathrm{pp} = 150$, the phase space becomes highly irregular. The initially distinct phase holes smear out as the distribution functions of protons and alpha particles coalesce and share the phase space. The lower fraction of the proton population in velocity space prevails, unlike the alpha population, which is fully captured by the complex particle dynamics in the trapping range.

4.2 Simulation convergence

Here, we run simulations of the same nominal plasma conditions while varying the number of pseudoparticles N_sim. The goal is to figure out how many pseudoparticles we need at minimum to accurately represent the real plasma dynamics. The wave properties predicted by the linear theory based on the dispersion relation in section 2.2.2 serve as a reference which should be exact in the linear regime. Thus, we take them as the ground truth. Deviations from the theoretical predictions indicate that the simulations have not converged fully at a given resolution.

Figure 4.5 shows the simulation estimates alongside the results from the dispersion relation. Note that the theoretical results do have very small errors $\epsilon \sim 10^{-4}$ which are not displayed and deemed negligible. Simulations with $N_\mathrm{sim}/N_\mathrm{cell} = 2^5$ and $N_\mathrm{sim}/N_\mathrm{cell} = 2^6$ did not give reproducible results. In this regime, the noise levels of the electric field energy are on the order $\langle W_E \rangle_x \sim 10\,\mathrm{MeV}$. This is above the maximum electric field energy measured in all simulations with higher pseudoparticle numbers (cf. fig. 4.1). Consequently, we cannot determine a linear regime or measure wave properties. In conclusion, the results for such low particle numbers are inconsistent and will be discarded. Consistent wave growth is measured across all four runs for $N_\mathrm{sim}/N_\mathrm{cell} \geq 2^7$.

The normalized wave frequency $\omega_\mathrm{max}/\omega_\mathrm{pp}$ is displayed in fig. 4.5a. It converges to the theoretical results for $N_\mathrm{sim}/N_\mathrm{cell} \geq 2^8$. The error is limited by the temporal resolution of $\Delta t\omega_\mathrm{pp} = 0.2$ which means that we can meaningfully improve the accuracy of our measurements. Consequently, we will use a temporal resolution of at least $\Delta t\omega_\mathrm{pp} = 0.1$ at which we capture our simulations. Note that the actual timescales of the simulation are much smaller $\Delta t_\mathrm{sim}\omega_\mathrm{pe} \ll 1$.

Figure 4.5b shows the normalized wavenumber $k_\mathrm{max}\lambda_\mathrm{D}$. In principle, we can only measure $k_{\mathrm{max},x} = k_\mathrm{max}\cos\theta_\mathrm{max}$ in these one-dimensional simulations. However, due to the shallow angle $\theta_\mathrm{max} \approx 7°$, we approximate $k_{\mathrm{max},x} \approx k_\mathrm{max}$. Furthermore, the Debye length λ_D technically changes as the electron temperature changes. Even so, the changes are limited to below 1% ($T_e^{t=0} \sim 100\Delta T_e$). For an accurate comparison to the linear theory, we always calculate λ_D based on the initial temperatures. Simulation estimates of the wavenumber converge for $N_\mathrm{sim}/N_\mathrm{cell} \gtrapprox 2^9$. Here, run-to-run variance is the primary error source, while the systematic error due to the resolution limit of $\Delta k\lambda_\mathrm{D} = 0.5$ can be relevant in some cases. Nevertheless, we decide against increasing the spatial resolution as the systematic error of $\epsilon_\mathrm{sys} \approx 0.05$ is smaller

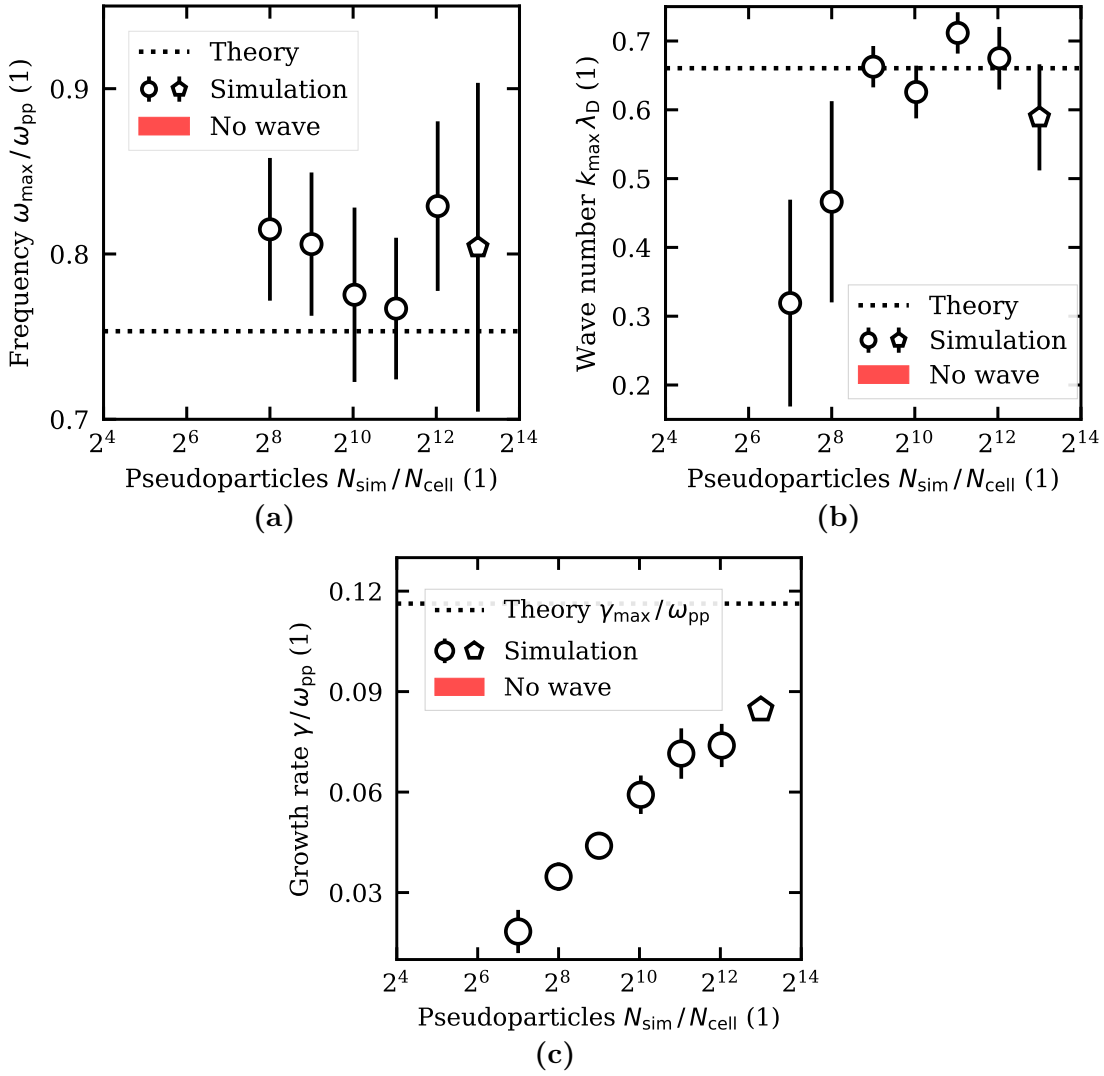

Figure 4.5: Dependence of the dominant **(a)** wave frequency, **(b)** wavenumber and **(c)** growth rate on the number of pseudoparticles per simulation cell N_{sim}/N_{cell}. Round markers signify four independent simulation runs at nominal conditions with different random seeds (cf. table 2.1). For the highest number of pseudoparticles only a single run is available (pentagon). The error bars indicate the sum of the systematic error due to the data resolution, and the statistical run-to-run error. For N_{sim}/N_{cell}, $\omega_{max}/\omega_{pp} \approx 8$ which is not shown in **(a)**.

than the estimated run-to-run error $\epsilon_{r2r} \approx 0.1$ for a single run. The magnitude of the run-to-run error implies that our decision avoids large computational costs for limited accuracy improvements.

Finally, the linear dispersion relation also predicts the growth rate γ_{max} of the wave. While it is possible to measure γ_{max} in the simulation (via the amplitude of the strongest growing mode), this measurement is quite noisy. Thus, we decide to measure the total growth rate via the electric field. This leads to an overestimate

of the growth rate in the simulation due to the approximation that a single mode with $\gamma = \gamma_{\max}$ dominates the spectrum ($\exists_j \forall_{i \neq j} \exp(\gamma_j) \gg \exp(\gamma_i)$):

$$\sum_i \exp(2\gamma_i t) \geq \exp(2\gamma_{\max} t). \tag{4.3}$$

Despite this overestimation, the comparison in fig. 4.5c reveals that growth rates in the simulation do not reach the predicted $\gamma_{\max}$. One reason for the significant underestimation in our simulations could be related to the principle on which we base our calculations of γ. Namely, we assume that the slope of the region in which the mean electric field energy $\langle W_E \rangle_x$ grows linearly is representative for the growth rate. However, it is possible that even in this regime, non-linear effects meaningfully impact the plasma dynamics. These can dampen the wave growth compared to the instantaneous growth rate in the theory. While it is possible that such deviations from linear theory depend on the plasma parameters, any physically accurate simulation can never depend on $N_{\text{sim}}/N_{\text{cell}}$. Unfortunately, even up to $N_{\text{sim}}/N_{\text{cell}} = 2^{13}$, it remains unclear whether our growth rate estimates converge to a different limit value near $\gamma = 0.09$. Thus, simulations with even higher $N_{\text{sim}}/N_{\text{cell}}$ are necessary to determine when convergence occurs. Due to the large computational cost of those simulations, we decide to abort our exploration at $N_{\text{sim}}/N_{\text{cell}} = 2^{13}$ and accept that we may not achieve convergence for γ specifically.

While the theoretical predictions are limited to the linear regime, we can also easily check the convergence of the plasma heating. Figure 4.6c displays the heating in the drift direction against $N_{\text{sim}}/N_{\text{cell}}$. We observe that the heating for all particle species converges for $N_{\text{sim}}/N_{\text{cell}} \geq 2^9$ with some variations due to run-to-run variance. This indicates that the long-term evolution of the instability converges even when the specific dynamics during the growth phase are not yet settled.

Let us summarize: In the simulation, $\omega_{\max}/\omega_{\text{pp}}$ and $k_{\max}\lambda_{\text{D}}$ converge toward theoretical predictions for $N_{\text{sim}}/N_{\text{cell}} = 2^9$. However, even up to $N_{\text{sim}}/N_{\text{cell}} = 2^{13}$, the simulation growth rate is significantly lower than expected from linear theory and steadily increases as $N_{\text{sim}}/N_{\text{cell}}$. Therefore, we will not focus on γ for most results in this work. The plasma heating of the simulations plateaus at $N_{\text{sim}}/N_{\text{cell}} = 2^9$. All in all, we decide to run our simulations with $N_{\text{sim}}/N_{\text{cell}} = 2^{10}$, $\Delta t \omega_{\text{pp}} = 0.1$ and $\Delta k \lambda_{\text{D}} = 0.5$.

4.3 Number density

Here, we present the results of a parameter sweep over the density ratio between protons and alpha particles n_α/n_{p}. We do this such that the plasma remains charge neutral $2\,n_\alpha + n_{\text{p}} = n_{\text{e}}$ and the electron density $n_{\text{e}} = 12\,\text{cm}^{-3}$ as well as other parameters remain at nominal plasma conditions (cf. table 2.1). The theoretical results in fig. 2.3 (a) are displayed from $n_\alpha/n_{\text{p}} = 10^{-3}$ to $n_\alpha/n_{\text{p}} = 10^{1}$. In the simulations, we find that the time to reach the linear regime depends strongly on the chosen density ratio. Figure 4.7a shows that for small density ratios $n_\alpha/n_{\text{p}} \ll 1$, the simulations remain close to the noise floor for a long time. Additionally, the low alpha particle density n_α also implies that the energy of the alpha distribution W_α

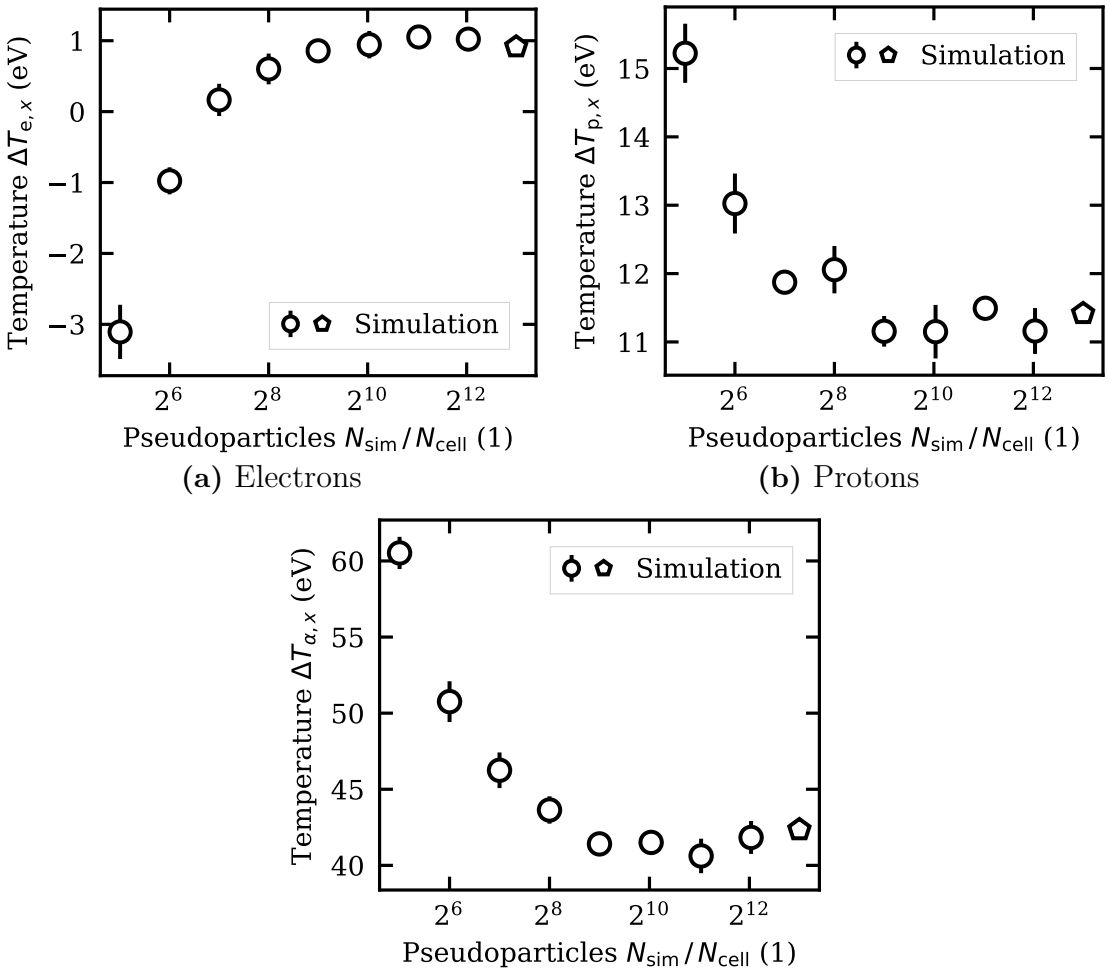

(a) Electrons **(b)** Protons **(c)** Alpha particles

Figure 4.6: Dependence of the temperature increase in the x-direction $\Delta T_{s,x}$ of the particle species on the number of pseudoparticles per simulation cell $N_{\mathrm{sim}} \,/\, N_{\mathrm{cell}}$. For the highest number of pseudoparticles only a single run is available (pentagon). Round markers signify four independent simulation runs at nominal conditions with different random seeds (cf. table 2.1). The errors are based on run-to-run variance, as statistical errors are negligible.

is small. Consequently, the available energy for the wave growth is limited. This effectively decreases the signal-to-noise ratio in the simulation, which forces us to simulate with higher $N_{\mathrm{sim}}/N_{\mathrm{cell}}$. Here, we choose $N_{\mathrm{sim}}/N_{\mathrm{cell}} = 2^{13}$ and limit the parameter scan from $n_\alpha/n_\mathrm{p} = 10^{-1.75}$ which allows us to keep the simulation time at $t\,\omega_{\mathrm{pp}} = 150$. On the other end, simulations up to $n_\alpha/n_\mathrm{p} = 10^{-0.25}$ enable us to explore the plasma evolution at the highest growth rates.

In principle, we want to compare our simulations against theoretical predictions for the wave properties. However, for most density ratios, we fail to estimate both the wavenumber and the wave frequency with our technique (cf. section 4.1). The evolution of the electric field in fig. 4.8 illustrates the problem: The discretization noise in the simulation leads to spatial inhomogeneities in our domain. On the other

hand, we use the plane wave ansatz which assumes spatial homogeneity in the linear theory. When the plane wave approximation is no longer applicable, modes can grow with varying strength depending on the local perturbations. For example, in fig. 4.8 the first visible crests and troughs appear at $x/\lambda_\mathrm{D} \approx 50$ and $t\,\omega_\mathrm{pp} \approx 15$. However, around $x/\lambda_\mathrm{D} \approx 32$ the first features appear at $t\,\omega_\mathrm{pp} \approx 30$ when a large part of the domain is already similar to the non-linear regime in fig. 4.1. We come to the conclusion that the domain is never globally in the linear regime required to measure the wave properties.

The mean electric field energy still contains a regime where it grows exponentially. Figure 4.7b shows that the growth rates γ measured in the simulation follow a similar trend as their theoretical predictions. While interesting, this result should be treated with caution because the numerical experiments in fig. 4.5c suggest that the growth rate has not converged. There is no confirmation that our simulations underestimate the theoretical prediction systematically across plasma parameters.

Figures 4.9a, 4.9b and 4.9c show the heating of the particle species. In section 4.1, we show that the vast majority of the plasma heating takes place during the linear growth phase. However, temperatures continue to increase into the non-linear regime. This trend continues across different density ratios. Thus, we measure the initial temperature and the temperature after a fixed delay of $t\omega_\mathrm{pp} = 44$ after the linear regime. This avoids a bias in the comparison of temperature differences, as the onset times vary for different density ratios (cf. fig. 4.7a). We can see that the heating increases together with the density ratio n_α/n_p up to $n_\alpha/n_\mathrm{p} \approx 10^{-0.5}$. At

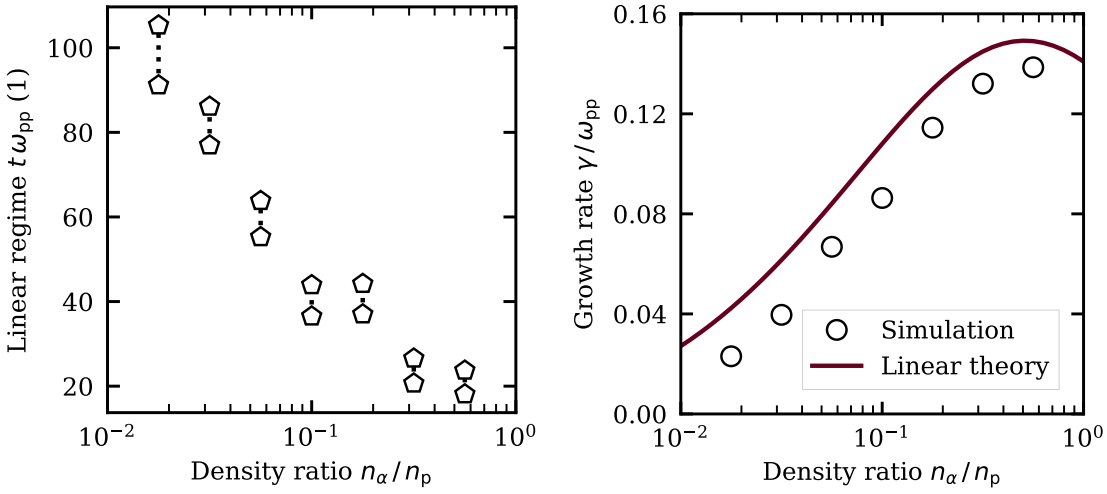

(a) **(b)**

Figure 4.7: Subplot **(a)** shows the length of the time range classified as the linear regime against the density ratio n_α/n_p. Subplot **(b)** shows the fitted growth rate in the simulation against the theoretical predictions in fig. 2.3 (a) via the dispersion relation (cf. eq. (2.14)). All simulations are one-dimensional under otherwise nominal plasma conditions (cf. table 2.1) with $N_\mathrm{sim}/N_\mathrm{cell} = 2^{13}$.

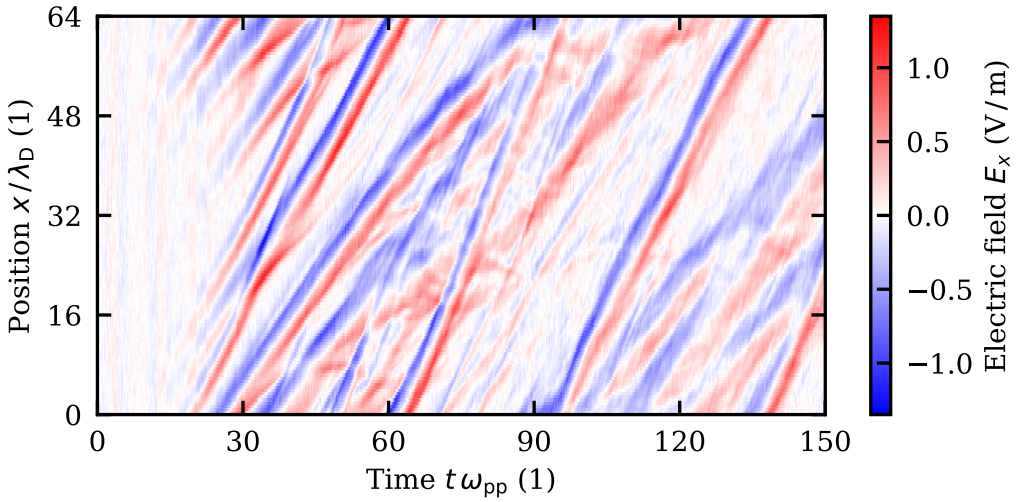

Figure 4.8: The spatio-temporal evolution of the electric field $E_x(x,t)$ for a density ratio of $n_\alpha/n_\mathrm{p} = 10^{-0.25}$ under otherwise nominal plasma conditions (cf. table 2.1) in a one-dimensional simulation.

$n_\alpha/n_\mathrm{p} \approx 10^{-0.25}$, the proton and alpha particle heating levels off while the electron temperatures continue to increase. Overall, the heating follows a similar trend as the growth rates.

Finally, we can understand the transfer of energy away from the alpha particles due to the instability. We observe that the alpha particles lose the largest fraction of their energy $\Delta W_\alpha/W_\alpha^{t=0} \approx 0.26$ at $n_\alpha/n_\mathrm{p} \approx 10^{-0.75}$ (not shown). Figure 4.9d shows how this energy is distributed throughout the system depending on the density ratio n_α/n_p after the linear growth phase. Note that much longer simulations are required to judge the long-term energy distribution ($W_E/W_\mathrm{total} \ll 1$). At low n_α/n_p, most of the energy remains in the electric field even until the end of the simulation period. As n_α/n_p increases, a larger fraction of energy is transferred to the protons. The electrons also receive an increasing fraction of the energy. However, it remains significantly less compared to the protons ($\Delta W_\mathrm{e} \ll \Delta W_\mathrm{p}$) for all density ratios. Overall, fig. 4.9d suggests that the timescale of instability critically depends on the density ratio.

4.4 Alpha particle flow velocity

This section concerns the dependence of the instability characteristics on the alpha flow velocity u_α. For simplicity and due to the inherent symmetries of the system[2], we limit ourselves to a variation over $u_\alpha = u_{\alpha,x}$.

Initially, we discuss the wave properties, which we can once again compare with the linear theory from the dispersion relation (cf. fig. 2.3). Figure 4.10a shows that

[2]The drift velocity of the alphas is the only parameter that breaks isotropy in the unmagnetized case.

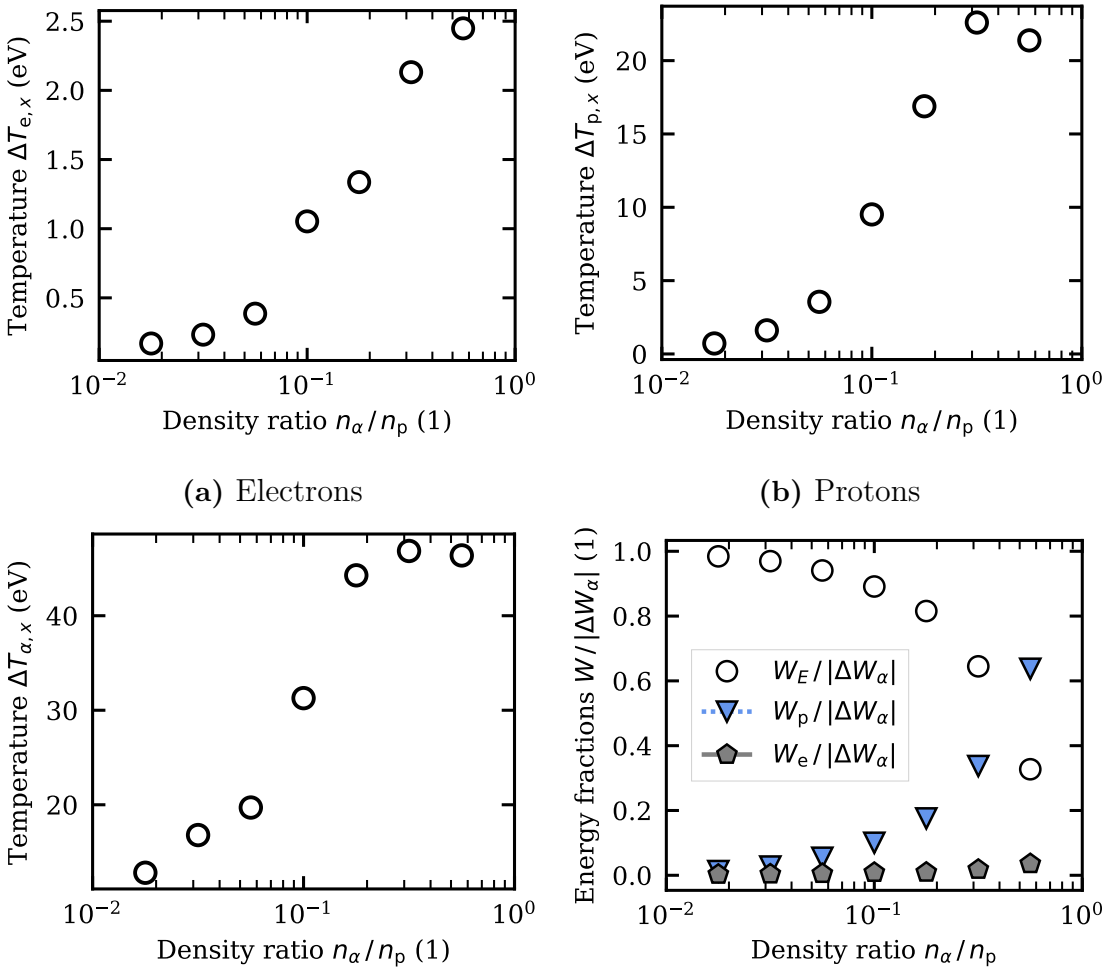

(a) Electrons **(b)** Protons

(c) Alpha particles **(d)**

Figure 4.9: Heating of **(a)** electrons, **(b)** protons, and **(c)** alpha particles for different density ratios n_α/n_p at otherwise nominal plasma conditions (cf. table 2.1). Subplot **(d)** shows the partition of the lost alpha particle energy in the frame of the initial proton flow. In both cases, the temporal difference is measured between the start of the simulation and $t\,\omega_{pp} = 44$ after the end of the linear regime, as for $n_\alpha/n_p = 10^{-1.75}$ we reach the end of the simulation period.

the wave frequency is overall similar to the theoretical predictions for low and high drift velocities. While this is within one standard deviation, the simulation values seem to slightly overestimate frequencies compared to linear theory. Furthermore, we observe that the estimation is independent of the component of the electric field, i.e. we obtain the same ω_{max} when using E_x and E_y. This is expected and underpins the physical adequacy of our method. A major deviation from theoretical predictions is visible around $u_\alpha \approx 150\,\mathrm{km/s}$. Here, the frequency is significantly reduced. We currently do not have a satisfying answer as to why this occurs. One possible reason is a strong spatial perturbation similar to those discussed in section 4.3. In that case, another mode at $\omega \neq \omega_{max}$ can dominate the system if it starts with an

initially much higher amplitude. However, the power spectral densities (in simulation and dispersion relation) at $u_\alpha = 150\,\mathrm{km/s}$ and $u_\alpha = 160\,\mathrm{km/s}$ do not show any strong secondary modes. Furthermore, such a specific spatial perturbation is statistically extremely unlikely. Note, however, that this type of anomaly would directly affect the phase velocity. Since we do not observe any corresponding changes in the evolution of the distribution functions, this points to an issue with our estimation scheme for ω.

The normalized wavenumber is shown in fig. 4.10b. Again, the simulation results agree well with the predictions from the dispersion relation. Similar to the results of the wave frequency, the simulations tend to produce slightly higher estimates compared to their theoretical counterpart. Here, no anomaly is visible around $u_\alpha = 140\,\mathrm{km/s}$ or $u_\alpha = 150\,\mathrm{km/s}$ and results based on E_x and E_y are very similar.

The results for the growth rate γ have to be treated with caution, as we did not reach convergence in section 4.2. Nevertheless, we can note that the growth rates remain constant for changing flow velocities with fluctuations below 10 %. Their mean remains at $\gamma/\omega_{\mathrm{pp}} \approx 0.08$ which is significantly below the theoretical prediction of $\gamma_{\mathrm{max}}/\omega_{\mathrm{pp}} \approx 0.11$ which is somewhat expected from fig. 4.5c.

Overall, the deviations from linear theory for k_{max} and ω_{max} are likely due to the temporal and spatial resolution being limited. Additionally, the discretization noise in the simulation can lead to slightly asymmetric growth of nearby modes. Figure 4.11 shows a snapshot of the electric field towards the end of the linear regime. While less severe than in fig. 4.8, these intricate curved and asymmetric transitions between crests and troughs suggest significant non-linear effects which put the plane

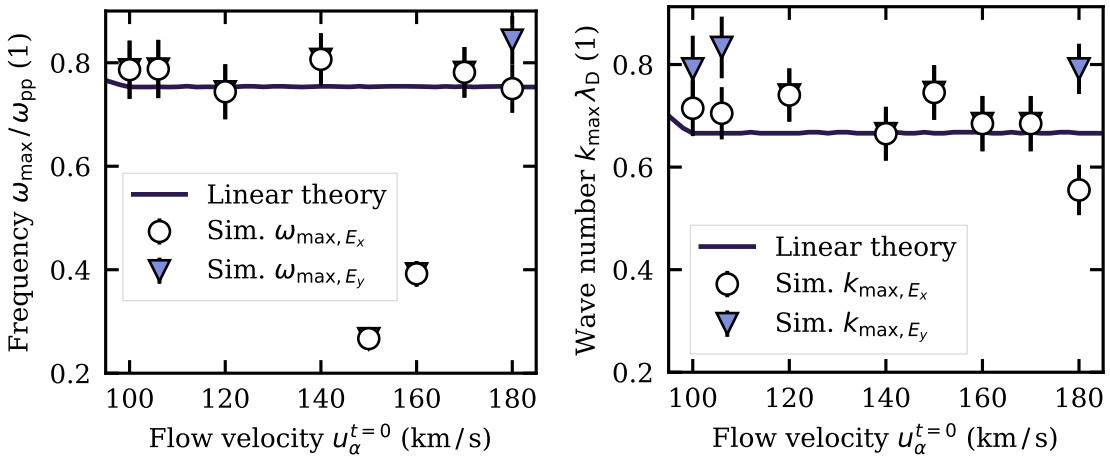

(a) **(b)**

Figure 4.10: Estimates of frequency and wavenumber are compared with linear theory for different flow velocities u_α. The theoretical results are identical to fig. 2.3 (b) via the dispersion relation in eq. (2.14). The simulation estimates are obtained from two-dimensional simulations under otherwise nominal plasma conditions (cf. table 2.1).

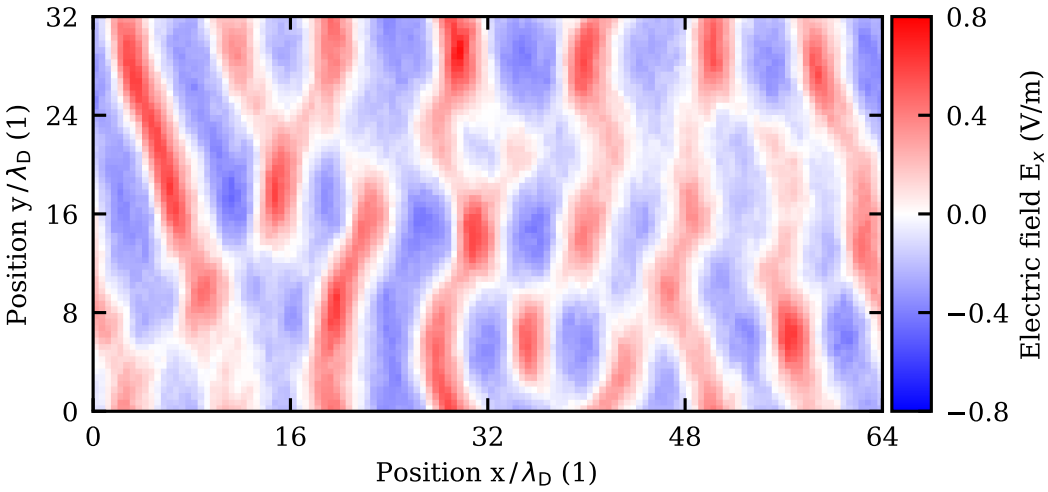

Figure 4.11: Snapshot of the spatially resolved electric field E_x during the linear regime at $t\,\omega_{\mathrm{pp}}$ for a two-dimensional simulation at nominal plasma conditions (cf. table 2.1). The electric field E_y is weaker but has a similar structure and is not shown here.

wave approximation into question. It is expected that simulations at much higher particle numbers $N_{\mathrm{sim}}/N_{\mathrm{cell}}$ would reduce these effects, since the corresponding lower initial noise level would allow a longer linear growth phase. This in turn leads to a clearer separation of linear modes growing with similar growth rates.

Since the simulations over the flow velocity u_α are two-dimensional, we can measure the angle between the propagation direction of the wave and the drift direction θ_{max}. Figure 4.12 shows the theoretical predictions together with simulation estimates via both $\boldsymbol{k}$ and $\boldsymbol{E}$ directly. Here, we calculate $\boldsymbol{k}_{\mathrm{max}}$ as outlined in section 4.1 via the discrete Fourier transform of E_x. Subsequently, we compute θ_{max} based on geometrical considerations:

$$\theta_{\mathrm{max}} = \arctan\left(\frac{k_{\mathrm{max},y}}{k_{\mathrm{max},x}}\right). \tag{4.4}$$

In addition, we may also use $E_{\mathrm{rms},x}$ and $E_{\mathrm{rms},y}$ in eq. (4.4) instead of $k_{\mathrm{max},x}$ and $k_{\mathrm{max},y}$, respectively. This calculation is justified through Faraday's law for electrostatic waves, which implies $\boldsymbol{k} \times \boldsymbol{E} = 0$. Figure 4.12 shows that both estimates agree well with the predictions from the linear theory in fig. 2.3 (b). Most likely, the estimates via $\boldsymbol{E}$ deviate from the theory again because of the non-linear effects. These increase the electric field strength perpendicular to the phase velocity of the wave (cf. fig. 4.11) which results in a systematic bias. This bias is strong for small wave angles, where E_y is expected to be close to zero in the plane wave approximation. On the other hand, the estimate via $\boldsymbol{k}$ would be strongly affected only if these non-linearities are particularly effective around a specific wavenumber. Thus, we believe that the estimate via $\boldsymbol{k}$ is generally more robust than via $\boldsymbol{E}$ but it is fundamentally limited by the k-space resolution which results in larger uncertainties for small wave angles θ_{max}.

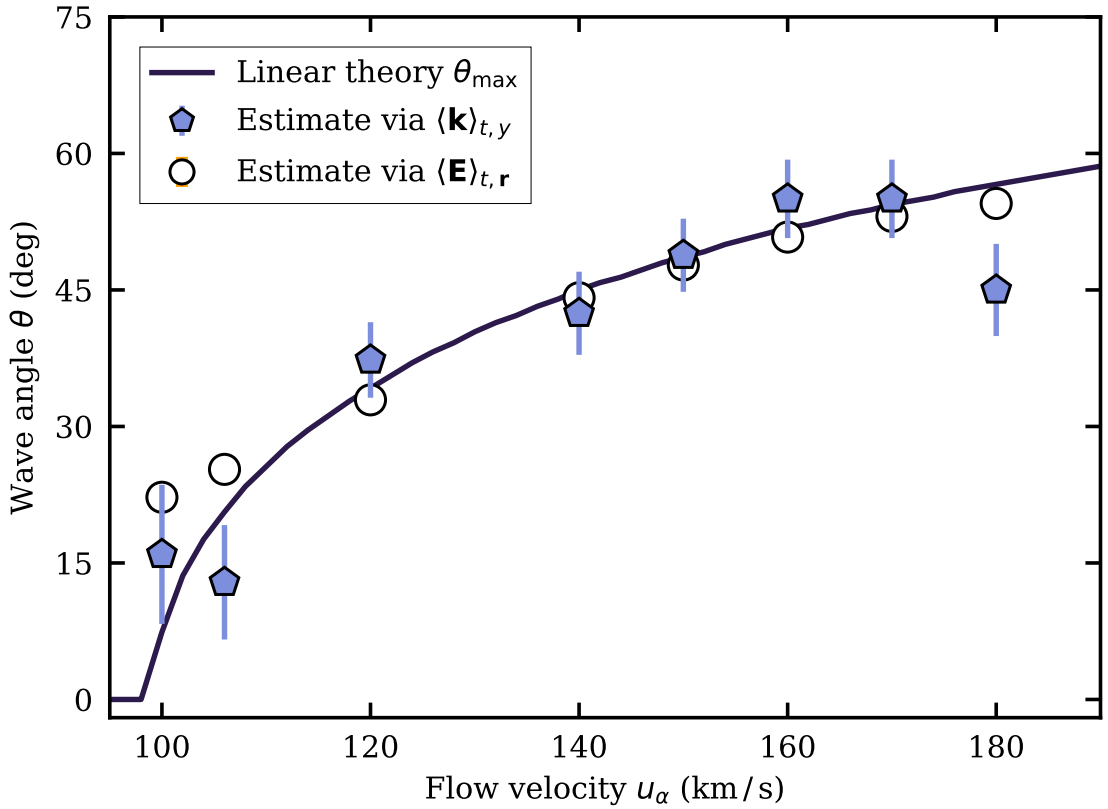

Figure 4.12: Wave angle estimates are compared with linear theory for different flow velocities u_α. The theoretical results of $\theta_{\max}$ are those from fig. 2.3 (b) via the dispersion relation in eq. (2.14). The simulation estimates are obtained from two-dimensional simulations under otherwise nominal plasma conditions (cf. table 2.1).

We combine the wave angle together with the trapping region of the Landau resonance to understand the evolution of the distribution functions f_α and f_p in velocity space. Figure 4.13 shows the proton and alpha VDFs at the end of the linear regime and at the end of the simulation. Note that we do not show the initial distributions because we already know that they will be approximately Maxwellian with radial symmetry around their respective flow velocity. At the end of the linear growth phase, both distributions have evolved significantly from their initial state. However, their changes are highly structured. The trapping regions originate in linear Landau theory (cf. section 2.1.2). It broadly reflects the part of the phase in which the Landau resonance (at that time) influences particles of a given species.

This picture directly corresponds to fig. 4.13 (a) and (b): Outside the trapping regions (transparent bands) the distributions remain almost identical to their initial state. They are rotationally symmetric with increasing density towards the initial flow velocity $u_s^{t=0}$ (white dot with black edge). On the other hand, inside the trapping region, particles are redistributed across their band (indicated by the black arrows). This leads to the formation of two wide branches away from the centre of the distribution, which abruptly stop at the end of the trapping region. Further-

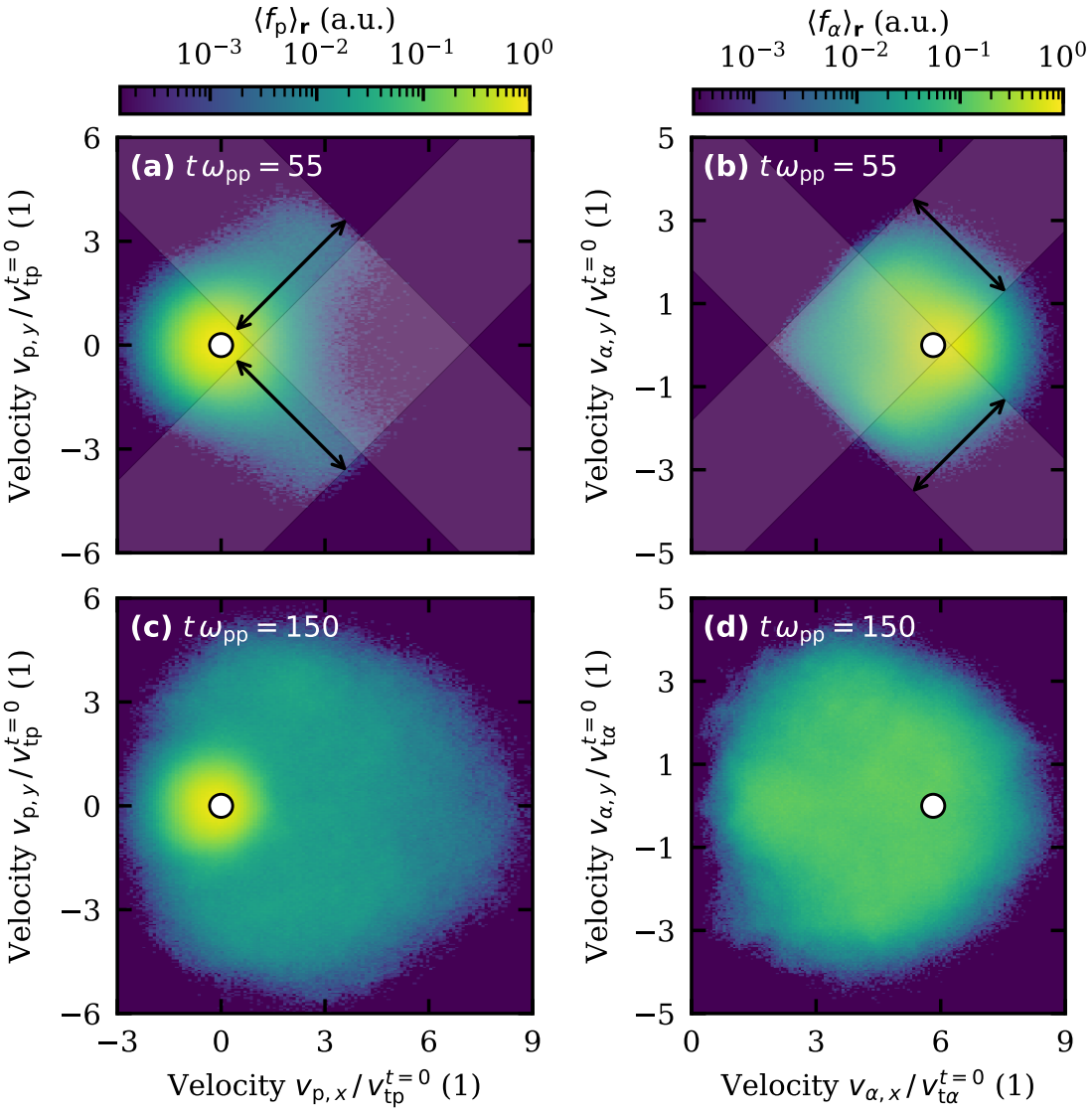

Figure 4.13: The spatially averaged distribution functions of protons, **(a)** and **(c)**, alpha particles, **(b)** and **(d)**, are shown in velocity space for $u_\alpha = 140\,\mathrm{km/s}$ and otherwise nominal conditions (cf. table 2.1). The white dots indicate the centre of the distribution functions at $t\omega_{pp} = 0$. The semi-transparent bands in **(a)** and **(b)** show the location a size of the trapping region based on θ_{max} from the theory and the maximum electric potential ϕ in the simulation at $t\omega_{pp} = 55$ (end of the linear regime). The black arrows indicate the direction of particle transport in the velocity space of the corresponding band.

more, we observe a region in the shape of a rhombus, where the two bands overlap. This region always occurs for non-zero wave angles $\theta_{\max} > 0$ but its location and size depends on $\theta_{\max}$ (or equivalently u_α) and the species charge-to-mass ratio. Here, particles are transported in both directions. For the alpha distribution in fig. 4.13 (a), the rhombus contains the centre of the distribution. Consequently, many particles are redistributed all throughout. For the protons, however, the overlap region is located away from the centre and the density remains low up until the end of the linear regime. The evolution of the VDFs displayed in fig. 4.13 (a) and (b) is generally representative for all simulations in the flow velocity variation. Nevertheless, a change in the wave angle $\theta_{\max}$ also modifies the angle between the trapping regions (it is $\pi/2 - \theta_{\max}$), and thus the location of the overlap region.

Figure 4.13 (c) and (d) show the VDFs at the end of the simulation period. Here, the plasma dynamics are highly non-linear, and it is evident that the redistribution of particles is no longer constrained to the trapping ranges shown in fig. 4.13 (a) and (b). Nevertheless, both distributions remain mirror symmetric with respect to the x-axis. The proton VDF in fig. 4.13 (c) develops a wide plateau that stretches primarily towards high velocities in the beam direction ($v_{\mathrm{p},x}/v_{\mathrm{tp}} \gg 0$). This reflects an increase in flow velocity $u_{\mathrm{p},x} > 0$. On the other hand, the alpha distribution loses kinetic energy, i.e. its drift velocity decreases significantly ($u_\alpha < u_\alpha^{t=0}$). While the alpha distribution appears completely flat ($u_\alpha^{t=0}$ is no longer visible), the proton distribution retains a visible maximum around $u_{\mathrm{p}}^{t=0}$.

Finally, fig. 4.14 displays the plasma heating for the different species. First and foremost, it is clear that the temperatures increase for all species over all simulated flow velocities u_α. While protons and alpha particles heat up drastically, fig. 4.14 (a) shows that the electron temperature is barely affected (cf. section 4.1). Furthermore, we notice that the heating increases as the flow velocity of the alpha particles increases. This is not surprising, as the flow velocity directly determines the kinetic energy of the alphas, and thus the total available energy. Due to this overall trend, it is more interesting to look at the normalized heating $\Delta T_s / K_\alpha^{t=0}$ which is shown in the right column of fig. 4.14. Here, we notice that the largest proton and alpha heating occurs at u_α where the wave angle is at $\theta_{\max} \approx 45°$ (cf. fig. 4.12). Notably, the electron heating in fig. 4.14 (b) does not appear to follow the same trend.

The origin of this particular relationship between the plasma heating and the flow velocity is difficult to determine exactly. However, we suspect that it is directly related to the geometry and location of the trapping regions relative to the VDF of the respective species (cf. fig. 4.13). As $\theta_{\max}$ or rather the flow velocity u_α increases, the two bands in fig. 4.13 rotate into a more horizontal position. This simultaneously covers a larger fraction of the proton distribution f_{p} and moves their overlap region into the centre of the alpha distribution. The increased spread in the distributions increases their temperature. At the same time, however, the fraction of the proton distribution which may be covered by these bands is limited geometrically by their width, which ultimately restricts the possible temperature increases.

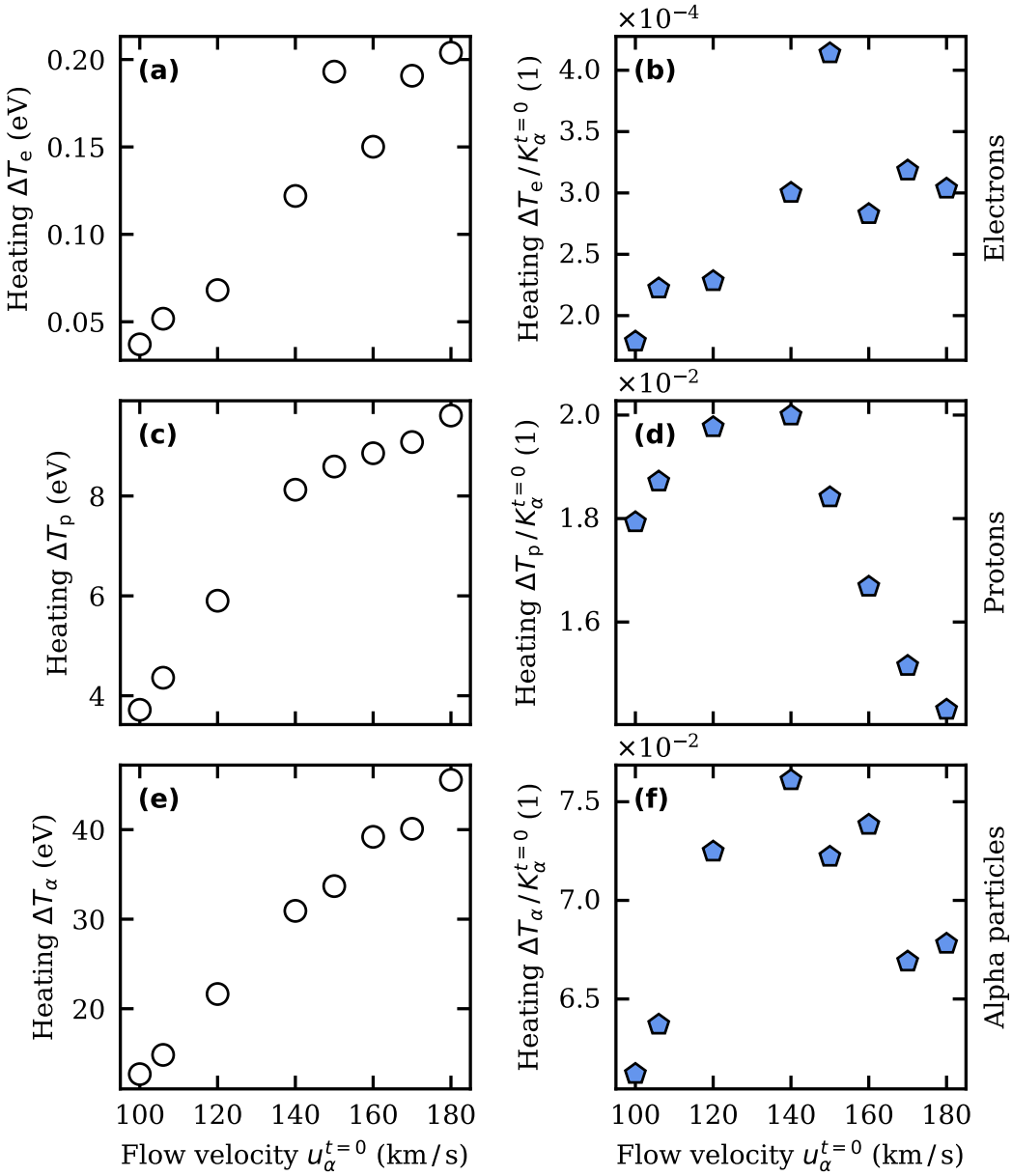

Figure 4.14: Dependence of the plasma heating for individual particle species on the flow velocity u_α over the entire simulation period. Subplots **(a)**, **(c)**, and **(e)** show the heating in physical units. Subplots **(b)**, **(d)**, and **(f)** show the heating normalized by the initial kinetic energy of the alphas. All values are obtained from two-dimensional simulations under otherwise nominal plasma conditions (cf. table 2.1).

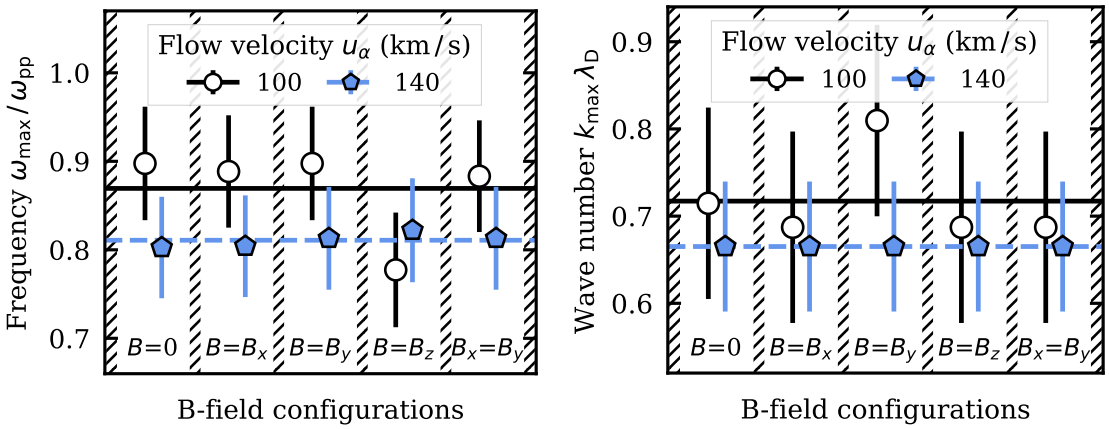

Figure 4.15: Estimates of frequency and wavenumber for different magnetic field directions at $B = 45\,\mathrm{nT}$. The values at alpha flow velocity $u_\alpha = 100\,\mathrm{km/s}$, and $u_\alpha = 140\,\mathrm{km/s}$ are offset relative to each other to improve visibility. The horizontal lines represent the mean value between all runs. The diagonal hatch patterns separate simulations with different magnetic field directions. All simulations are two-dimensional and have otherwise nominal plasma conditions (cf. table 2.1).

4.5 Background magnetic fields

The results from the dispersion relation and the description via linear theory in section 2.2.2 are only valid in a purely electrostatic setting, where the background magnetic field vanishes ($\boldsymbol{B}_0 = 0$). Here, we test the validity of that assumption through our simulations for a background magnetic field with a field strength of $B = 45\,\mathrm{nT}$. This magnetic field strength is representative of the magnetic fields measured by the MMS mission's spacecrafts near the bow shock (Graham et al., 2025).

Figure 4.15 shows the wave properties of simulations with different magnetic field configurations, as well as without any magnetic field. Solely for $u_\alpha = 100\,\mathrm{km/s}$, the wave frequency for the case $B = B_z$ and the wavenumber for the case $B = B_y$ differ slightly. However, both changes correspond to a shift of only $\Delta k\lambda_\mathrm{D} = 0.5$ or $\Delta\omega/\omega_\mathrm{pp} = 0.1$, respectively, which represent the resolution limit of the simulation. Chi-squared tests at each flow velocity have p-values of $p > 0.6$ for both the wave frequency and wavenumber. This confirms that there is no statistical difference between the wave properties at different magnetic field settings for either flow velocity. This result can be understood via the gyrofrequencies ω_{cs} of the different species:

$$\omega_{cs} = \frac{|q_s|B}{m_s}. \tag{4.5}$$

At the current magnetic field strength, both the proton and the alpha gyrofrequencies are extremely small. This means that their gyration periods are very large

compared to the typical timescales of the instability. For $B = 45\,\mathrm{nT}$, we can calculate that the alpha particles will rotate by less than 30° and protons less than 60° over the entire simulation period ($t\,\omega_{\mathrm{pp}} = 150$). Only the electron gyrofrequency is similar to the timescale of the instability $\omega_{\mathrm{ce}} \approx 2\omega_{\mathrm{pp}}$. Since the linear growth phase ends at $t\,\omega_{\mathrm{pp}} \approx 50$ and the electrons are not strongly affected by the Landau resonance, the influence of the magnetic field is minimal.

The limited impact of the magnetic field, as expected from the low ion gyrofrequencies, is also seen in terms of the ion heating. Figure 4.16 shows how the plasma heating of the different particle species changes relative to their heating in the absence of a magnetic field. The electron heating, which is generally quite small, increases by approximately a factor four when the magnetic field is perpendicular to the drift direction of the alpha particles ($B = B_y$). For the case $B = B_x$, the increase in plasma heating is minimal, while the case $B_x = B_y$ lies somewhere in between. At $u_\alpha = 140\,\mathrm{km/s}$, the difference in heating between $B = B_x$, $B_x = B_y$ and $B = B_y$ suggests that the heating increases proportionally to B_y. The proton and alpha particle heating is reduced only slightly to approximately 90% of the original value. The decrease in temperature depends both on the magnetic field direction and the flow velocity u_α. Unfortunately, no clear trend can be inferred. All in all, we expect the heating to be further suppressed at increasing magnetic field strength. This can be intuitively understood as follows: For simplicity, let us consider a magnetic field $B = B_z$. In this case, the alpha VDF essentially is in a constant rotation in the $x - y$-plane (cf. fig. 4.13 (b) and fig. 2.4b). This also continuously changes the location and geometry of the trapping region(s) which hinders wave growth. Thus, the instability is suppressed.

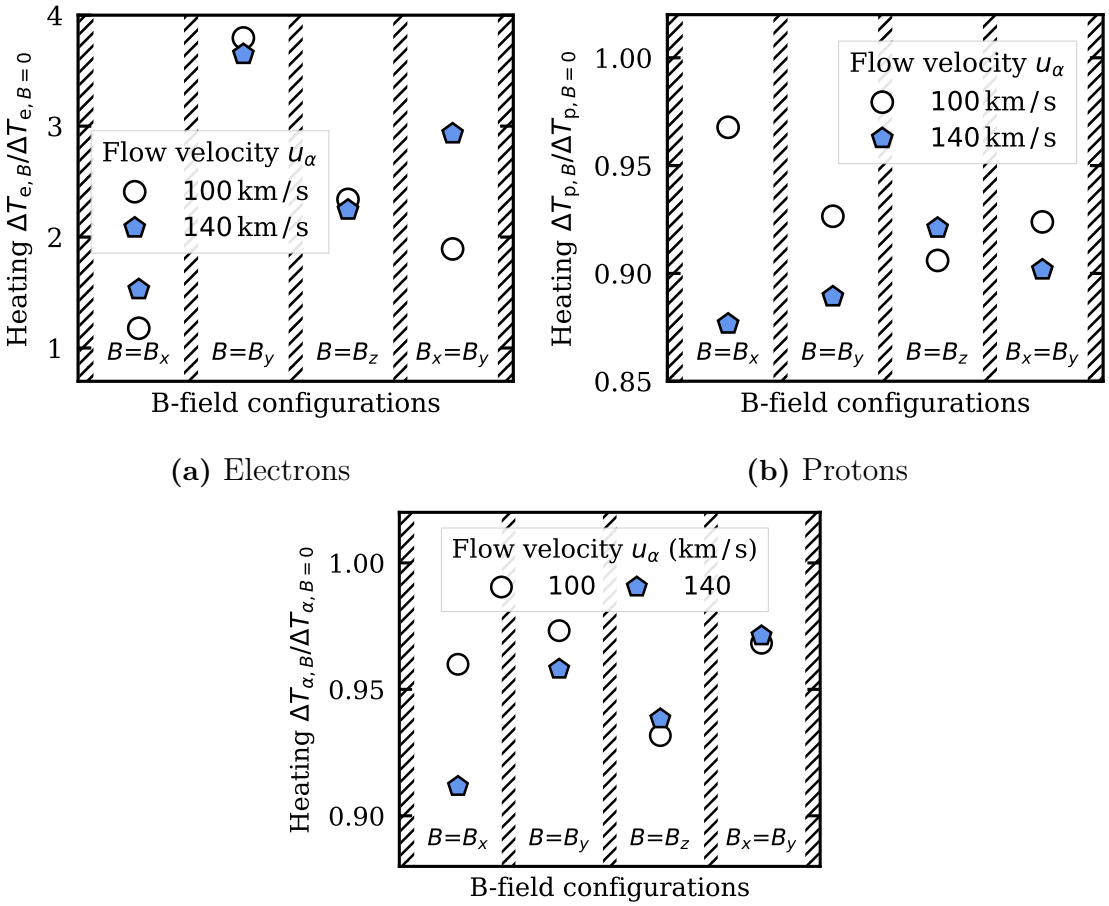

(a) Electrons

(b) Protons

(c) Alphas

Figure 4.16: Dependence of the plasma heating of the particle species on the magnetic field direction at $B = 45\,\mathrm{nT}$ and alpha flow velocities $u_\alpha = 100\,\mathrm{km/s}$, and $u_\alpha = 140\,\mathrm{km/s}$. The diagonal hatch patterns separate simulations with different magnetic fields. All simulations are two-dimensional and have otherwise nominal plasma conditions (cf. table 2.1).

5

Conclusion

The Earth's bow shock is a region in front of the Earth, where the solar wind is abruptly slowed down due to its interaction with the planetary magnetic field. This environment provides a unique opportunity to study and characterize a natural collisionless plasma. The complex and dynamic environment of the Earth's bow shock supports a variety of plasma waves, representing an intensive field of study. Recently, a streaming instability between protons and alpha particles has been observed just downstream of the shock. It leads to the formation of large-amplitude ion-acoustic-like waves, which heat the plasma. In this thesis, we study the non-linear evolution of the proton-alpha instability and its dependencies on plasma parameters.

EPOCH, a fully kinetic Particle-In-Cell (PIC) code, solves the non-linear Vaslov-Maxwell equations self-consistently via a Lagrangian approach. It allows us to capture and investigate the spatial and temporal evolution of the plasma via the distribution functions of the different particle species and the electromagnetic fields. The number of simulated particles presents the primary constraint to the accuracy of our simulation. In this work, we use at least 2^{10} pseudoparticles per cell. For the spatial and temporal resolution, we choose $\Delta k \lambda_D = 0.5$ and $\Delta t\, \omega_{\mathrm{pp}} = 0.1$ which allow measurements of wavenumber and frequency at reasonable accuracy. Note that the actual timescale of the simulations is limited by the CFL condition with $\Delta t_{\mathrm{sim}} \omega_{\mathrm{pe}} \ll 1$. A periodic domain of at least 128 (1D simulations) or 64×32 (2D simulations) grid cells is chosen to reduce the influence of box modes.

In a first step, we used one-dimensional simulations to show that the dominant frequency and wavenumber of the plasma waves converge to their predictions from the linear dispersion relation in theory. The final simulation temperatures are found to be independent of the number of pseudoparticles at our simulation parameters. While we could not achieve convergence for the growth rate at bearable computational costs, we expect that the observed parametric dependencies on other plasma properties hold.

Access to the full distribution functions enables important insights into the dynamics of electrons, protons, and alpha particles throughout the instability. We find that electrons are only marginally affected with temperature increases on the order of 1%. The change in protons and alpha particle distributions is consistent with expectations on Landau growth from theory and literature. Both species experience significant plasma heating, which appears predominantly in the direction of the phase velocity of the wave. The vast majority of that heating takes place during the linear growth phase of the instability.

In one-dimensional simulations, we vary the density ratio between protons and alpha particles $n_\alpha / n_{\mathrm{p}}$. Unfortunately, a comparison of the wave properties to theo-

retical predictions turns out to be difficult. We attribute this to non-linear effects enhanced by spatial inhomogeneities due to the discretization noise in our simulations. In the future, higher fidelity simulations, or a different estimation method for the wave properties may be used to check the consistency with linear theory. Despite convergence issues with the wave's growth rate, we find that theoretical predictions and simulation estimates follow a similar trend. Overall, the plasma heating after the linear growth phase increases significantly at higher growth rates. At the same time, the distribution of the energies in the system changes with the density ratio. For $n_\alpha/n_\mathrm{p} \ll 1$, most of the energy is stored in the electric field. On the other hand, as $n_\alpha/n_\mathrm{p} \to 1$, the kinetic energy of the alphas is immediately converted to plasma heating. Overall, this indicates that the density ratio critically affects the timescale of the proton-alpha instability. Future simulations could be used to determine the energy composition over much longer timescales in the non-linear regime.

Even at non-zero flow velocities of the alpha particles u_α, the system retains a rotational symmetry around the drift direction (in the unmagnetized case). Consequently, two-dimensional simulations are sufficient to investigate the parametric dependence of the plasma on u_α. We find that the wavenumber and wave angle, i.e. the angle between the drift direction and the phase velocity, are consistent with linear theory. While the wave's frequency mostly agrees with the theory, there are two significant outliers whose origin remains unclear. At the same time, the distribution functions in those simulations do not deviate from expectations via Landau theory. This suggests that our estimation method is potentially insufficient to identify the correct frequencies. An increase of the flow velocity u_α directly corresponds to a higher kinetic energy in the system. As such, the plasma heating across species rises with u_α. Notably, it does so in a non-linear fashion. Instead, the maximum heating compared to the available energy occurs at a 45° wave angle. We suspect that this is connected to the geometry of the instability in velocity space. The location of wave's trapping region changes for different flow velocities, which effectively constraints the change in distribution functions and therefore the plasma heating.

Finally, we find that background magnetic fields with similar strength as in the Earth's bow shock have a minor influence on the instability. The heating of the ions is slightly suppressed, but the wavenumber and frequency are not affected. Electron heating increases but is limited to a few percent of the initial electron temperature. Overall, the influence of the magnetic field is primarily due to an interaction with the electrons: Only the electron cyclotron frequency is comparable to the proton plasma frequency and thus the timescales of the instability. On the other hand, the ion gyration timescales are orders of magnitude larger than proton plasma frequency. Generally, the observed change in heating depends on the strength and the direction of the background magnetic field.

In future research, it would be interesting to investigate the non-linear dynamics over longer timescales, as this would significantly improve the understanding of the long-term energy composition of the system. Furthermore, some theoretical work can be done to unambiguously determine the relationship between the plasma heating and the flow velocity u_α.

Data availability

All simulations were performed with the openly available EPOCH code (Arber et al., 2015). The data analysis and plots were made in Python 3. The corresponding scripts or rather the source code is hosted at https://github.com/insalt-glitch/proton-alpha-instability-simulations.

Bibliography

Arber, T D et al. (Nov. 2015). 'Contemporary particle-in-cell approach to laser-plasma modelling'. In: *Plasma Physics and Controlled Fusion* 57.11, pp. 1–26. DOI: 10.1088/0741-3335/57/11/113001.

Balogh, André and Rudolf A. Treumann (2013). *Physics of Collisionless Shocks: Space Plasma Shock Waves*. Vol. 12. Springer New York, NY. ISBN: 978-1-46146098-5. DOI: 10.1007/978-1-4614-6099-2.

Bame, S. J. et al. (Feb. 1968). 'Solar Wind Ion Composition'. In: *Physical Review Letters* 20.8, pp. 393–395. ISSN: 0031-9007. DOI: 10.1103/physrevlett.20.393.

Birdsall, C.K. and A.B Langdon (Oct. 2018). 'Plasma Physics via Computer Simulation'. In: DOI: 10.1201/9781315275048.

Burch, J. L. et al. (May 2015). *Magnetospheric Multiscale Overview and Science Objectives*. DOI: 10.1007/s11214-015-0164-9. URL: https://mms.gsfc.nasa.gov/.

Coburn, Jesse T., Christopher H.K. Chen and Jonathan Squire (Sept. 2022). 'A measurement of the effective mean free path of solar wind protons'. In: *Journal of Plasma Physics* 88.5. ISSN: 1469-7807. DOI: 10.1017/S0022377822000836.

Cohen, Ian J. et al. (June 2019). 'High-Resolution Measurements of the Cross-Shock Potential, Ion Reflection, and Electron Heating at an Interplanetary Shock by MMS'. In: *Journal of Geophysical Research: Space Physics* 124.6, pp. 3961–3978. ISSN: 2169-9402. DOI: 10.1029/2018ja026197.

Courant, R., K. Friedrichs and H. Lewy (Dec. 1928). 'Über die partiellen Differenzengleichungen der mathematischen Physik'. In: *Mathematische Annalen* 100.1, pp. 32–74. ISSN: 1432-1807. DOI: 10.1007/bf01448839.

Davidson, P. A. (Mar. 2001). 'An Introduction to Magnetohydrodynamics'. In: DOI: 10.1017/CBO9780511626333.

Dijk, J van, G M W Kroesen and A Bogaerts (Sept. 2009). 'Plasma modelling and numerical simulation'. In: *Journal of Physics D: Applied Physics* 42.19, p. 190301. ISSN: 1361-6463. DOI: 10.1088/0022-3727/42/19/190301.

Engquist, B., J. Häggblad and O. Runborg (Sept. 2012). 'On energy preserving consistent boundary conditions for the Yee scheme in 2D'. In: *Bit Numer. Math.* 52.3, pp. 615–637. ISSN: 1572-9125. DOI: 10.1007/s10543-012-0376-2.

Freidberg, Jeffrey P. (June 2014). *Ideal MHD*. Cambridge University Press. ISBN: 9780511795046. DOI: 10.1017/cbo9780511795046.

Fried, Burton D. and Samuel D. Conte (2015). *Plasma Dispersion Function The Hilbert Transform of the Gaussian. The Hilbert Transform of the Gaussian*. Elsevier Science & Technology Books. ISBN: 9781483261737.

Fuselier, S. A. and W. K. H. Schmidt (June 1994). 'H+ and He2+ Heating at the Earth's bow shock'. In: *Journal of Geophysical Research: Space Physics* 99.A6, pp. 11539–11546. ISSN: 0148-0227. DOI: 10.1029/94ja00350.

Gary, S. Peter (Apr. 1979). 'A second-order theory for the ion-acoustic heat flux instability'. In: *Journal of Plasma Physics* 21.2, pp. 361–379. ISSN: 1469-7807. DOI: 10.1017/s0022377800021917.

Graham, D. B., Yuri V. Khotyaintsev and Ahmad Lalti (2025). 'Ion-Acoustic Waves and the Proton-Alpha Streaming Instability at Collisionless Shocks'. In: DOI: 10.48550/ARXIV.2502.07953.

Graham, D. B. et al. (Apr. 2024). 'Ion Dynamics Across a Low Mach Number Bow Shock'. In: *J. Geophys. Res. Space Phys.* 129.4, e2023JA032296. ISSN: 2169-9380. DOI: 10.1029/2023JA032296.

Kennel, C. F., J. P. Edmiston and T. Hada (Jan. 1985). 'A Quarter Century of Collisionless Shock Research'. In: *Collisionless Shocks in the Heliosphere: A Tutorial Review*. Chichester, England, UK: John Wiley & Sons, Ltd., pp. 1–36. ISBN: 978-1-11866403-2. DOI: 10.1029/GM034p0001.

— (Mar. 2013). 'A Quarter Century of Collisionless Shock Research'. In: pp. 1–36. ISSN: 2328-8779. DOI: 10.1029/gm034p0001.

Kennel, C. F. and F. Engelmann (Dec. 1966). 'Velocity Space Diffusion from Weak Plasma Turbulence in a Magnetic Field'. In: *The Physics of Fluids* 9.12, pp. 2377–2388. ISSN: 0031-9171. DOI: 10.1063/1.1761629.

Kunimune, Justin (Dec. 2023). *landau-damping*. Online. URL: https://github.com/jkunimune/landau-damping.

Lalti, A. et al. (Aug. 2022). 'A Database of MMS Bow Shock Crossings Compiled Using Machine Learning'. In: *Journal of Geophysical Research: Space Physics* 127.8. ISSN: 2169-9402. DOI: 10.1029/2022ja030454.

Landau, L (1946). 'On the vibrations of the electronic plasma'. In: *Zhurnal eksperimentalnoi i teoreticheskoi fiziki* 16.7, pp. 574–586. DOI: 10.1016/B978-0-08-010586-4.50066-3.

Merka, J. et al. (Apr. 2005). 'Three-dimensional position and shape of the bow shock and their variation with upstream Mach numbers and interplanetary magnetic field orientation'. In: *Journal of Geophysical Research: Space Physics* 110.A4. ISSN: 0148-0227. DOI: 10.1029/2004ja010944.

Neugebauer, Marcia and Conway W. Snyder (Oct. 1966). 'Mariner 2 observations of the solar wind: 1. Average properties'. In: *Journal of Geophysical Research* 71.19, pp. 4469–4484. ISSN: 0148-0227. DOI: 10.1029/jz071i019p04469.

Owens, Mathew J. (Feb. 2020). 'Solar-Wind Structure'. In: *Oxford Research Encyclopedia of Physics*. Oxford University Press. DOI: 10.1093/acrefore/9780190871994.013.19.

Parker, E. N. (Nov. 1958). 'Dynamics of the Interplanetary Gas and Magnetic Fields.' In: *The Astrophysical Journal* 128, p. 664. ISSN: 1538-4357. DOI: 10.1086/146579.

Paschmann, G. et al. (Sept. 1980). 'Energization of solar wind ions by reflection from the Earth's bow shock'. In: *Journal of Geophysical Research: Space Physics* 85.A9, pp. 4689–4693. ISSN: 0148-0227. DOI: 10.1029/ja085ia09p04689.

Pollock, C. et al. (Mar. 2016). 'Fast Plasma Investigation for Magnetospheric Multiscale'. In: *Space Science Reviews* 199.1-4, pp. 331–406. ISSN: 1572-9672. DOI: 10.1007/s11214-016-0245-4.

Swanson, D. G. (2003). *Plasma waves*. Institute of Physics Publishing, p. 456. ISBN: 075030927X.

Tonks, Lewi and Irving Langmuir (Feb. 1929). 'Oscillations in Ionized Gases'. In: *Physical Review* 33.2, pp. 195–210. ISSN: 0031-899X. DOI: 10.1103/physrev.33.195.

Tooley, C. R. et al. (Nov. 2015). 'The Magnetospheric Multiscale Constellation'. In: *Space Science Reviews* 199.1-4, pp. 23–76. ISSN: 1572-9672. DOI: 10.1007/s11214-015-0220-5.

Webb, David F. and Timothy A. Howard (Dec. 2012). 'Coronal Mass Ejections: Observations'. In: *Living Rev. Sol. Phys.* 9.1, pp. 1–83. ISSN: 1614-4961. DOI: 10.12942/lrsp-2012-3.

Yee, Kane (1966). 'Numerical solution of initial boundary value problems involving maxwell's equations in isotropic media'. In: *IEEE Transactions on Antennas and Propagation* 14.3, pp. 302–307. DOI: 10.1109/TAP.1966.1138693.

DEPARTMENT OF PHYSICS
CHALMERS UNIVERSITY OF TECHNOLOGY
Gothenburg, Sweden
www.chalmers.se

CHALMERS
UNIVERSITY OF TECHNOLOGY